

1 **TITLE: Organelle proteomic profiling reveals lysosomal heterogeneity in association with**  
2 **longevity**

3

4 **AUTHOR:** Yong Yu<sup>1,2, #,\*</sup>, Shihong M. Gao<sup>3,4, #</sup>, Youchen Guan<sup>4,5, #</sup>, Pei-Wen Hu<sup>2</sup>, Qinghao  
5 Zhang<sup>2</sup>, Jiaming Liu<sup>1</sup>, Bentian Jing<sup>1</sup>, Qian Zhao<sup>2</sup>, David M Sabatini, Monther Abu-Remaileh<sup>6,8</sup>,  
6 Sung Yun Jung<sup>7</sup>, Meng C. Wang<sup>2,4,\*</sup>

7

8 1. State Key Laboratory of Cellular Stress Biology, School of Life Sciences, Faculty of Medicine  
9 and Life Sciences, Xiamen University, Xiamen 361102, China

10 2. Huffington Center on Aging, Baylor College of Medicine, Houston TX, USA 77030

11 3. Developmental Biology Graduate Program, Baylor College of Medicine, Houston TX, USA  
12 77030

13 4. Janelia Research Campus, Howard Hughes Medical Institute, Ashburn VA, USA 20147

14 5. Molecular and Cellular Biology Graduate Program, Baylor College of Medicine, Houston TX,  
15 USA 77030

16 6. Department of Chemical Engineering and Genetics, Stanford University, Stanford CA, USA  
17 94305

18 7. Department of Molecular and Cellular Biology, Baylor College of Medicine, Houston TX,  
19 USA 77030

20 8. Institute for Chemistry, Engineering and Medicine for Human Health (ChEM-H), Stanford  
21 University, Stanford, CA 94305, USA

22

23 # Equal contribution

24 \* Correspondence and requests for materials should be addressed to Meng C. Wang

25 ([mengwang@janelia.hhmi.org](mailto:mengwang@janelia.hhmi.org)) or Yong Yu ([yuy@xmu.edu.cn](mailto:yuy@xmu.edu.cn))

26

27 **ABSTRACT**

28 Lysosomes are active sites to integrate cellular metabolism and signal transduction. A collection  
29 of proteins associated with the lysosome mediate these metabolic and signaling functions. Both  
30 lysosomal metabolism and lysosomal signaling have been linked to longevity regulation;  
31 however, how lysosomes adjust their protein composition to accommodate this regulation  
32 remains unclear. Using deep proteomic profiling, we systemically profiled lysosome-associated  
33 proteins linked with four different longevity mechanisms. We discovered the lysosomal  
34 recruitment of AMPK and nucleoporin proteins and their requirements for longevity in response  
35 to increased lysosomal lipolysis. Through comparative proteomic analyses of lysosomes from  
36 different tissues and labeled with different markers, we further elucidated lysosomal  
37 heterogeneity across tissues as well as the increased enrichment of the Ragulator complex on  
38 Cystinosin positive lysosomes. Together, this work uncovers lysosomal proteome heterogeneity  
39 across multiple scales and provides resources for understanding the contribution of lysosomal  
40 protein dynamics to signal transduction, organelle crosstalk and organism longevity.

41

42 **INTRODUCTION**

43

44 Lysosomes are membrane-bound organelles specialized to constitute an acidic environment in  
45 the cytosol. Lysosomes carry many proteins that are essential for maintaining lysosomal  
46 activities and mediating lysosomal regulatory effects. Inside the lysosomal lumen, a series of

47 acidic hydrolases, including lipases, proteases, glucosidases, acid phosphatases, nuclease and  
48 sulfatases, are responsible for the degradation and recycling of extracellular and intracellular  
49 materials delivered through endocytic, phagocytotic and autophagic processes (Appelqvist et al.,  
50 2013; Ballabio & Bonifacino, 2020; Lawrence & Zoncu, 2019). Additionally, on the lysosomal  
51 membrane, a group of integral transmembrane proteins play crucial roles in the maintenance of  
52 luminal acidic pH and ion homeostasis, the control of lysosomal membrane potential and export  
53 of metabolic products, as well as the regulation of organelle interaction and signal transduction  
54 (Ballabio & Bonifacino, 2020; Lawrence & Zoncu, 2019). For example, the lysosomal vacuolar-  
55 type H<sup>+</sup>-ATPase (v-ATPase) on the membrane is the primary driver for the active accumulation  
56 of protons in the lysosomal lumen, which also requires a neutralizing ion movement mediated by  
57 ion channels and transporters (Graves et al., 2008; Nicoli et al., 2019). In addition, v-ATPase  
58 coordinates with lysosomal amino acid transporter SLC38A9 and lysosomal cholesterol exporter  
59 NPC1 in regulating the activation of mechanistic/mammalian target of rapamycin complex I  
60 (mTORC1) by amino acid and lipid cues (Castellano et al., 2017; Wang et al., 2015). The  
61 recruitment of mTORC1 to the lysosome is mediated by RagA/B and RagC/D GTPase  
62 heterodimers that are associated with the scaffold protein complex Ragulator tethered on the  
63 lysosomal membrane (de Araujo et al., 2017). Through interacting with Axin, Ragulator also  
64 mediates the activation of AMP-activated protein kinase (AMPK) on the lysosomal surface  
65 (Zhang et al., 2014). Furthermore, lysosomes are not static, isolated organelles, instead they are  
66 highly mobile vesicles that undergo frequent movements in both anterograde (nucleus-to-  
67 periphery) and retrograde (periphery-to-nucleus) directions and form dynamic interactions with  
68 other organelles including endosomes, autophagosomes, endoplasmic reticulum and  
69 mitochondria (Ballabio & Bonifacino, 2020; Pu et al., 2016). These trafficking and interaction

70 processes are mediated by lysosomal integral transmembrane proteins as well as diverse proteins  
71 that are recruited to lysosomes in response to different extracellular and intracellular inputs  
72 (Ballabio & Bonifacino, 2020; Pu et al., 2016).

73

74 Lysosomes control numerous cellular processes, and dysfunction of lysosomes has been linked  
75 with various diseases, such as lysosomal storage disorders (Ballabio & Gieselmann, 2009; Platt  
76 et al., 2012), Alzheimer's disease (Nixon & Cataldo, 2006), Parkinson disease (Navarro-Romero  
77 et al., 2020) and some types of cancer (Davidson & Vander Heiden, 2017; Fehrenbacher &  
78 Jaattela, 2005). Emerging evidence also suggests that lysosome functions as a central regulator  
79 of organism longevity, through its involvement in autophagy and its modulation of metabolic  
80 signaling pathways. The induction of autophagic flux has been observed in multiple pro-  
81 longevity states, and is required for the pro-longevity effects caused by those genetic, dietary and  
82 pharmacological interventions, such as reduced insulin/IGF-1 signaling, caloric restriction, and  
83 spermidine treatment (Hansen et al., 2018). On the other hand, lysosomes are now recognized as  
84 the key platform to modulate the activities of mTORC1 and AMPK signaling, two well-  
85 characterized longevity regulating pathways (Savini et al., 2019). In addition, our studies have  
86 discovered lysosomal lipid messenger pathways that are induced by a lysosomal acid lipase  
87 LIPL-4 and promote longevity via both cell-autonomous and cell-nonautonomous signaling  
88 mechanisms (Folick et al., 2015; Ramachandran et al., 2019; Savini et al., 2022; Wang et al.,  
89 2008). Given the importance of lysosomes in regulating longevity, it will be crucial to  
90 understand how changes in the lysosomal protein composition are associated with longevity  
91 regulation.

92

93 To systemically profile the protein composition of lysosomes, methods have been developed to  
94 purify lysosomes using gradient centrifugation (Gao et al., 2017; Lubke et al., 2009; Markmann  
95 et al., 2017; Schroder et al., 2010). More recently, a lysosome immunoprecipitation method,  
96 which uses anti-HA (human influenza virus hemagglutinin) antibody conjugated magnetic beads  
97 to immuno-purify lysosomes from mammalian cells expressing transmembrane protein 192  
98 (TMEM192) fused with three tandem HA (3×HA) epitopes, has further improved the specificity  
99 and speed of lysosomal isolation (Abu-Remaileh et al., 2017). This rapid isolation method has  
100 facilitated follow-up mass spectrometry (MS)-based proteomics as well as metabolomics  
101 analyses (Abu-Remaileh et al., 2017; Eapen et al., 2021; Laqtom et al., 2022).

102

103 In the present study, we have applied an immunoprecipitation-based method for rapid isolation  
104 of lysosomes from live adult *C. elegans* using transgenic strains expressing lysosomal membrane  
105 proteins tagged with 3×HA (Lyso-Tag). We then conducted large-scale proteomic profiling using  
106 isolated lysosomes and remaining non-lysosomal fractions, to determine the enrichment of each  
107 identified protein on the lysosome. Based on these analyses, we have defined a lysosome-  
108 enriched proteome and compared it between wild-type and long-lived worms, revealing  
109 lysosomal protein composition changes associated with longevity. We have also generated  
110 transgenic strains expressing Lyso-Tag specifically in four major somatic tissues, the hypodermis  
111 (epidermis), muscle, intestine (digestive tract/fat tissue/liver) and neurons, leading to the  
112 discovery of lysosomal proteome heterogeneity in different tissues. Furthermore, by comparing  
113 the lysosome-enriched proteome with LAMP1/LMP-1 Lyso-Tag and the one with  
114 Cystinosin/CTNS-1 Lyso-Tag, we discovered that the Ragulator complex and other mTORC1

115 regulators exhibit increased enrichments on lysosomes containing the cysteine transporter  
116 Cystinosin.

117

118 **RESULTS**

119

120 **Map lysosome-enriched proteome systemically in *C. elegans***

121

122 To comprehensively reveal proteins that are enriched at the lysosome, we have applied rapid  
123 lysosome immunoprecipitation followed by MS-based proteomic profiling (Lyso-IP) (Figure 1A).  
124 We first generated a transgenic strain overexpressing the lysosome-associated membrane protein,  
125 LMP-1 (Eskelinne, 2006) fused to both 3×HA and RFP (LMP-1 *LysoTg*) under the whole-body  
126 *sur-5* promoter. Fluorescence imaging of RFP confirmed the lysosomal localization of the LMP-  
127 1 fusion protein in live organisms and made it possible to follow purified lysosomes *in vitro*  
128 (Figure 1B). The presence of transgenes does not affect worms' developmental timing and  
129 lifespan (Figure 1-figure supplement 1 A, B). The 3×HA epitope tag is used to purify lysosomes  
130 from homogenized worm lysate via immunoprecipitation using anti-HA antibody-conjugated  
131 magnetic beads (Figure 1A). In general, about 160,000 worms at day-1 adulthood were harvested  
132 and homogenized. Upon centrifugation to remove debris and nuclei, 3×HA-tagged lysosomes  
133 were immunoprecipitated and separated from other cellular content (flow-through controls,  
134 Figure 1A). The whole process from harvesting worms to purified lysosomes takes around 25  
135 minutes. Many purified lysosomes were able to take up LysoTracker probes and exhibit positive  
136 fluorescence signals, indicating that they remain intact with an acidic pH, while there are also  
137 some broken lysosomes losing LysoTracker staining (Figure 1C). When blotting with antibodies

138 against different organelle markers, we found that the purified lysosomes show no or nearly no  
139 protein markers of other organelles, including HSP-60 (mitochondria heat shock protein) (Hartl  
140 et al., 1992; Mayer, 2010), CYP-33E1 (Endoplasmic Reticulum (ER) cytochrome P450) (Brown  
141 & Black, 1989), SQV-8 (Golgi glucuronosyltransferase) (Hadwiger et al., 2010) and beta-actin  
142 (cytoskeleton) (Figure 1D), while the flow-through controls show these protein markers but  
143 nearly no lysosomal protein marker LMP-1 (Figure 1D). Together, these results demonstrate the  
144 efficacy of the Lyso-IP approach to enrich lysosomal proteins.

145

146 Next, we conducted proteomic profiling of purified lysosomes with their paired flow-through  
147 controls (Figure 1A). The correlation analysis shows good reproducibility among four  
148 independent biological replicates (Figure 1-figure supplement 1C), and the PCA analysis shows  
149 a clear separation between Lyso-IP replicates and flow-through controls (Figure 1E). In parallel,  
150 we also conducted immunoprecipitation using homogenized lysate from wild-type (WT) worms  
151 that do not carry a Lyso-Tag and then analyzed proteomic profiles of three independent samples  
152 as non-tag controls (Figure 1A).

153

154 Based on these proteomic data, we used three criteria to define lysosome-enriched proteins: first,  
155 their levels in the purified lysosomes are 10-fold or higher than those in the flow-through  
156 controls (Figure 2A); second, their enrichments can be repeated in all biological replicates  
157 (Figure 2A); and lastly, their enrichments over non-tag controls are more than 2-fold (Figure 2B).  
158 Together, 216 lysosome-enriched candidates were identified from more than 6000 detected  
159 proteins, and 178 candidates have mammalian homologs (Figure 2-figure supplement 1,  
160 Supplementary File 1). This lysosome-enriched proteome consists of 83 membrane transporters

161 and channels, 47 enzymes, 26 signaling factors, 12 structural components, and 6 involved in  
162 vesicle trafficking (Figure 2C). These include known lysosomal proteins, such as various  
163 lysosomal Cathepsins that catalyze protein degradation (Turk et al., 2012), lysosomal specific  
164 ARL8 GTPase that mediates lysosome trafficking (Nakae et al., 2010), and subunits of  
165 lysosomal v-ATPase that pumps protons into the lysosomal lumen to maintain an acidic pH  
166 (Forgac, 2007) (Supplementary File 1).

167

168 Lysosomal v-ATPase consists of both V0 and V1 domains that are associated with the lysosomal  
169 membrane and face the cytosol, respectively (Figure 2D). Reversible dissociation of the V1 and  
170 V0 domains responds to nutritional signals and plays a crucial role in the regulation of the  
171 lysosomal v-ATPase activity (Kane, 1995; McGuire & Forgac, 2018; Ratto et al., 2022; Stransky  
172 & Forgac, 2015). Except for VHA-18 (V1 H subunit), we were able to detect all other subunits  
173 of lysosomal v-ATPase, including VHA-5, 6, 7 and UNC-32 (V0 a subunits), VHA-1, 2, 3 and 4  
174 (V0 c subunits), VHA-16 (V0 d subunit), VHA-17 (V0 e subunit), VHA-13 (V1 A subunit),  
175 VHA-12 (V1 B subunit), VHA-11 (V1 C subunit), VHA-14 (V1 D subunit), VHA-8 (V1 E  
176 subunit), VHA-9 (V1 F subunit), VHA-10 (V1 G subunit), and VHA-15 (V1 H subunit), and  
177 also two v-ATPase transporting accessory proteins, VHA-19 and VHA-20 (Figure 2D,  
178 Supplementary File 1). Among the V0 domain subunits, VHA-4, 5, 6, 7 and 16 and UNC-32 are  
179 enriched over 10-fold in all four replicates, VHA-1, 2 and 3 are enriched over 10-fold in three  
180 replicates and over 5-fold in one replicate, and the low abundant VHA-17 was only detected in  
181 two replicates, with more than 10-fold enrichments in both (Figure 2D). The VHA-19  
182 transporting accessory protein is enriched over 10-fold in two replicates and less than 5-fold in  
183 two replicates (Figure 2D). In contrast, for the subunits of the V1 domain and the VHA-20

184 transporting accessory protein, they show no enrichment in the purified lysosomes compared to  
185 the flow-through controls (Figure 2D). These results suggest that the free form of the V1 domain  
186 and the associated form bound with the V0 domain at lysosomes both exist under well-fed  
187 condition in wild-type worms.

188

189 In addition to 30.7% of proteins with known lysosome/endosome localization, the lysosome-  
190 enriched proteome includes a small portion of proteins localized to other cellular organelles,  
191 ER/Golgi (6.0%), mitochondria (1.4%), peroxisome (0.4%), lipid droplet (0.9%), and synaptic  
192 vesicle (1.8%) (Figure 2E). On the other hand, there is a large portion of proteins with annotated  
193 plasma membrane localization (24.8%) (Figure 2E). Many of these plasma membrane proteins  
194 are receptors that are known to be subject to endocytosis and subsequent recycling lysosomal  
195 degradation, such as INA-1/integrin alpha-6 (De Franceschi et al., 2015), VER-3/vascular  
196 endothelial growth factor receptor (Ewan et al., 2006), PTC-1/protein patched receptor (Gallet &  
197 Therond, 2005), and IGLR-2/leucine-rich repeat-containing G-protein coupled receptor (Snyder  
198 et al., 2013) (Supplementary File 1) (Bräulke & Bonifacino, 2009). We also identified proteins  
199 involved in the endocytosis process, including low-density lipoprotein receptor-related proteins,  
200 LRP-1 (Grant & Hirsh, 1999) and arrestin domain-containing proteins, ARRD-13 and ARRD-18  
201 (Kang et al., 2014) (Supplementary File 1) that mediate the internalization of plasma membrane  
202 receptors (Ma et al., 2002). Thus, the lysosome-enriched proteome also reveals membrane  
203 receptor proteins that undergo recycling through the endo-lysosomal system.

204

205 **Profile lysosome-enriched proteome heterogeneity among different tissues**

206

207 Lysosomes are known as a heterogeneous population of vesicles, differing in their size, shape,  
208 pH and cellular distribution. They broadly exist in all tissues of an organism and play diverse  
209 roles in a tissue-specific manner. To examine how lysosome-enriched proteomes exhibit  
210 heterogeneity among different tissues, we have generated four transgenic strains that overexpress  
211 LMP-1 Lyso-Tag specifically in neurons, muscle, intestine, and hypodermis using tissue-specific  
212 promoters, *unc-119*, *myo-3*, *ges-1*, and *col-12*, respectively (Figure 3A). Using these transgenic  
213 strains, we purified lysosomes in a tissue-specific manner and conducted proteomic profiling.  
214 The correlation analysis shows good reproducibility among three independent biological  
215 replicates (Figure 3-figure supplement 1 A-D).

216

217 Unlike the whole-body Lyso-IP, the flow-through samples from tissue-specific Lyso-IP contain  
218 not only non-lysosomal fractions from the targeted tissue but also lysosomes from non-targeted  
219 tissues. Thus, these flow-through samples cannot be simply used as controls to determine the  
220 enrichment of proteins at the lysosome in the targeted tissue. To assess tissue-specific changes,  
221 we have normalized the level of each identified protein to the level of LMP-1 in the same  
222 replicate, and then compared the normalized ratio between the whole-body Lyso-IP and the  
223 tissue-specific Lyso-IP (Figure 3B-E, Supplementary File 2). We found that among the 216  
224 proteins identified from the whole-body Lyso-IP, 85 of them show comparable ratios between  
225 the whole-body Lyso-IP and the four tissue-specific Lyso-IPs (Figure 3F, Group I), suggesting  
226 relative homogenous lysosomal enrichments of these proteins among different tissues. Nine of  
227 them were completely absent in the tissue-specific Lyso-IP, which may be related to their low  
228 abundance (Figure 3F, Group IV).

229

230 Furthermore, there are 122 proteins that exhibited significant differences in their enrichments  
231 between the whole-body Lyso-IP and the tissue-specific Lyso-IPs ( $p < 0.05$ ), 56 of them (Group  
232 II) showing an increase in the tissue-specific Lyso-IPs while the other 66 (Group III) showing a  
233 decrease (Figure 3F). One of the candidates in Group II is Y58A7A.1, a copper uptake  
234 transporter, that shows a higher ratio in the hypodermis (Figure 3F). Copper transporters are  
235 crucial players in various biological processes and copper dysfunction contributes to oxidative  
236 stress, impaired respiration and enzymic activities, and disease progression. To validate whether  
237 Y58A7A.1 is a copper transporter specifically localized at the lysosome in the hypodermis, we  
238 generated a CRISPR knock-in line where the endogenous Y58A7A.1 is tagged with  
239 mNeonGreen. Using this line, we confirmed the hypodermis-specific lysosomal localization of  
240 Y58A7A.1 (Figure 3-figure supplement 1 E).

241

242 These results show that the lysosomal proteome exhibits heterogeneity among different tissues  
243 within the organism, which may be related to the metabolic status in each tissue and,  
244 consequently, contribute to the specific activities and signaling effects of the tissue. Our studies  
245 provide a list of candidates for further investigation into the tissue-specific regulation of  
246 lysosomal metabolism and signaling.

247

#### 248 **Lysosome-enriched proteome alterations associate with different pro-longevity mechanisms**

249

250 Considering the emerging role of lysosomes as a cellular hub to integrate protein signals and  
251 regulate longevity, we next examined whether the protein composition of lysosomes exhibits  
252 heterogeneity in association with different longevity mechanisms. To this end, we crossed LMP-

253 1 LysoTg with four different long-lived strains: the *lipl-4* transgenic strain (*lipl-4 Tg*) that  
254 constitutively expresses a lysosomal acid lipase (Wang et al., 2008), the loss-of-function mutant  
255 of *daf-2* (*daf-2(lf)*) that encodes the insulin/IGF-1 receptor (Kenyon et al., 1993; Martins et al.,  
256 2016), the loss-of-function mutant of *isp-1* (*isp-1(lf)*) that reduces mitochondrial electron  
257 transport chain complex III activity (Feng et al., 2001), and the *glp-1* loss-of-function mutant  
258 (*glp-1(lf)*) that has a defective germline at 25 °C non-permissive temperature (Berman & Kenyon,  
259 2006) (Figure 4A). We then conducted Lyso-IP proteomic analyses and compared lysosome-  
260 enriched proteomes between wild-type and long-lived strains. The correlation analysis shows  
261 good reproducibility among three independent biological replicates (Figure 4-figure supplement  
262 1 A-D), and the PCA analysis shows a clear separation between Lyso-IP replicates and flow-  
263 through controls (Figure 4-figure supplement 1 E, F).

264

265 In the *lipl-4 Tg* worms, we have identified 449 lysosome-enriched proteins (Supplementary File  
266 3), and 176 of them overlap with the candidates from WT worms (Figure 4B). Thus, 82% of  
267 proteins enriched on WT lysosomes are also enriched on *lipl-4 Tg* lysosomes; however, 61% of  
268 proteins enriched on *lipl-4 Tg* lysosomes are absent in WT lysosomes (Figure 4B). In parallel,  
269 259 lysosome-enriched proteins were identified in the *daf-2(lf)* mutant using LMP-1 Lyso-IP  
270 (Supplementary File 4), 147 of them overlapping with the LMP-1 Lyso-IP candidates from WT  
271 worms, 197 of them overlapping with the LMP-1 Lyso-IP candidates from the *lipl-4 Tg* worms,  
272 and 55 unique to the *daf-2(lf)* mutant (Figure 4C). In the *isp-1(lf)* mutant, we identified 177  
273 lysosome-enriched proteins (Supplementary File 5). Among them, 26 candidates are unique to  
274 the *isp-1(lf)* mutant, while 107, 135 and 126 candidates overlap with those in the WT, *lipl-4 Tg*  
275 and *daf-2(lf)* worms, respectively (Figure 4C). Meanwhile, 200 lysosome-enriched proteins were

276 identified in the *glp-1(lf)* mutant (Supplementary File 6). When compared to the control worms  
277 growing at the same 25 °C temperature (Supplementary File 7), 43 were unique to the *glp-1(lf)*  
278 mutant, while 157 overlapped with WT candidates (Figure 4-figure supplement 1 G). Overall,  
279 there is only one lysosome-enriched candidate shared among all four long-lived strains but  
280 absent from the WT lysosome-enriched proteome (Figure 4-figure supplement 1 H), suggesting  
281 that distinct pro-longevity mechanisms influence the protein composition of the lysosome in their  
282 specific ways. Furthermore, for the long-lived *daf-2(lf)*, *isp-1(lf)* and *glp-1(lf)* worms, the  
283 overlaps of their lysosome-enriched proteome with the WT are 57%, 60% and 78.5% (Figure 4C,  
284 Figure 4-figure supplement 1 G), respectively. These percentages are higher than the 39%  
285 overlap observed between the long-lived *lipl-4 Tg* worms and the WT (Figure 4B). These results  
286 support that increased lysosomal lipolysis leads to bigger changes on lysosomal protein  
287 composition than other pro-longevity mechanisms.

288

289 In the *lipl-4 Tg*, *daf-2(lf)*, and the *glp-1(lf)* lysosome-enriched proteomes, we found the  
290 enrichment of autophagosome proteins and proteins that mediate the fusion between  
291 autophagosomes and lysosomes, including ATG-9/ATG9A (*lipl-4 Tg*, *daf-2(lf)*, and *glp-1(lf)*),  
292 SQST-1/SQSTM1 (*daf-2(lf)* and *glp-1(lf)*), EPG-7/RB1CC1 (*lipl-4 Tg*), VAMP-7/VAMP8 (*lipl-*  
293 *4 Tg*) and Y75B8A.24/PI4KIIα (*lipl-4 Tg*) (Figure 5A), which is consistent with the previously  
294 reported induction of autophagy in these long-lived conditions (Lapierre et al., 2011; Nakamura  
295 & Yoshimori, 2018);

296

297 In addition, we found that the Ragulator complex, LMTR-2/LAMTOR2, LMTR-3/LAMTOR3  
298 and LMTR-5/LAMTOR5, that serves as a scaffold for the activation of mTORC1 and AMPK

299 (Zhang et al., 2014), shows a higher enrichment at the lysosome from the *lipl-4* *Tg* worms than  
300 WT (Figure 5A). However, such increased enrichments were not detected in the lysosome from  
301 the *daf-2(lf)*, *isp-1(lf)* or *glp-1(lf)* mutant (Figure 5A). It is known that the Ragulator complex  
302 mediates the lysosomal activation of AMPK (Zhang et al., 2014). There are two homologs of  
303 AMPK catalytic units, AAK-1 and AAK-2 in *C. elegans*. We found that AAK-2 is enriched  
304 more than 10-fold in the Lyso-IP samples compared to the flow-through controls from the *lipl-4*  
305 *Tg* worms, but it is only detected in the flow-through controls from WT worms (Figure 5B).  
306 Likely due to its low abundance, AAK-1 was detected twice in the Lyso-IP samples from the  
307 *lipl-4* *Tg* worms but once only in the flow-through sample from WT worms (Figure 5B). On the  
308 other hand, AAK-1 and AAK-2 were not present in the lysosome-enriched proteome from the  
309 *daf-2(lf)*, *isp-1(lf)* or *glp-1(lf)* mutant (Figure 5B). These results suggest that AMPK is  
310 specifically recruited to the lysosomal surface in the *lipl-4* *Tg* worms, which may contribute to  
311 the pro-longevity effect. To test this idea, we inactivated AMPK using the *aak-2* loss-of-function  
312 mutant together with the *aak-1* RNA interference (RNAi) knockdown. We found that the AMPK  
313 inactivation reduces the lifespans of the *lipl-4* *Tg* and WT worms by 29% and 17%, respectively,  
314 and suppresses the lifespan extension caused by *lipl-4* *Tg* from 72% to 48% (Figure 5C,  
315 Supplementary File 8). Thus, *aak-1* and *aak-2* are partially responsible for the lifespan extension  
316 caused by *lipl-4* *Tg*. For the AMPK catalytic subunits, It is known that the activation of AMPK  
317 displays high spatial specificity in the cell when responding to different upstream stimuli (Khan  
318 & Frigo, 2017). In *C. elegans*, it was previously shown that AAK-2 mediates the longevity effect  
319 conferred by the *daf-2(lf)* mutant (Apfeld et al., 2004). Our results indicate that this regulation  
320 might not be associated with the lysosomal activation of AMPK, and the spatial specificity of

321 AMPK activation at different subcellular compartments may be linked with different longevity  
322 mechanisms.

323

324 Moreover, compared to WT lysosomes, the enrichment of lysosomal v-ATPase is higher in *lipl-4*  
325 *Tg* lysosomes, especially for the V0 subunits, VHA-1, 2, 3 the V1 subunits, VHA-11 and VHA-  
326 15, and the v-ATPase transporting accessory proteins, VHA-19 and VHA-20 (Figure 5A). There  
327 are also 13 lysosomal channels/transporters, including T14B4.3/ATP6AP2, the proton-  
328 translocating ATPases required for the v-ATPase-mediated lysosomal acidification (Cruciat et al.,  
329 2010) and CLH-6/CLCN7, the H(+)/Cl(-) exchange transporter mediating the acidification of the  
330 lysosome (Graves et al., 2008; Nicoli et al., 2019), and 16 lysosomal hydrolases that are  
331 specifically associated with the *lipl-4 Tg* lysosomes (Figure 5A). However, none of these  
332 components exhibit increased enrichments in the lysosome from the *daf-2(lf)*, *isp-1(lf)* or *glp-1(lf)*  
333 mutant (Figure 5A). Together, these results suggest that the proportion of mature acidic  
334 lysosomes may be increased in the *lipl-4 Tg* worms, which may lead to increased autophagy, the  
335 lysosomal activation of AMPK, and consequently the induction of longevity.

336

337 **Enhanced lysosome-nucleus proximity mediates longevity responding to lysosomal lipolysis**

338

339 It is known that the luminal pH of lysosomes is affected by their cellular position, with  
340 perinuclear lysosomes being more acidic (Johnson et al., 2016). In the cell, mobile lysosomes  
341 can change their distribution along the perinuclear-peripheral axis in response to different  
342 nutrient signals and metabolic status (Ballabio & Bonifacino, 2020; Pu et al., 2016). Interestingly,  
343 when analyzing the LMP-1 lysosome-enriched proteome in the *lipl-4 Tg* worms, we found an

344 enrichment of nucleus-localized proteins (Figure 6A), including two nucleoporin proteins NPP-  
345 6/Nup160 and NPP-15/Nup133 in the Nup160 complex that localizes at the basket side of the  
346 nuclear pore (Figure 6B) (Vasu et al., 2001). Such enrichment of nucleoporin proteins was not  
347 found in the LMP-1 lysosome-enriched proteome of the *daf-2(lf)*, *isp-1(lf)* or *glp-1(lf)* long-lived  
348 mutant. We thus hypothesize that LIPL-4-induced lysosomal lipolysis may increase the  
349 proximity between lysosomes and the nucleus, accompanied by an increase in lysosomal acidity.

350

351 To test this hypothesis, we imaged lysosomal positions in intestinal cells where *lipl-4* is  
352 expressed. Using a dual reporter strain expressing both lysosomal LMP-1::RFP fusion and  
353 nucleus-localized GFP, we found that lysosomes exhibit a dispersed pattern in the intestinal cell  
354 of WT worms (Figure 6C). However, in the *lipl-4* *Tg* worms, lysosomes are clustered in the  
355 perinuclear region (Figure 6C), supporting the hypothesis that the proximity between lysosomes  
356 and the nucleus is increased. To quantitatively measure this change in lysosomal positioning, we  
357 analyzed the RFP fluorescent signal distribution in intestinal cells (Figure 6-figure supplement 1  
358 A). We found the perinuclear and peripheral distribution of lysosomes in the *lipl-4* *Tg* worms is  
359 significantly increased and decreased, respectively, compared to WT worms ( $p < 0.01$ , Figure 6D,  
360 Figure 6-figure supplement 1 B). In contrast, such perinuclear clustering is not observed in  
361 intestinal cells of the *daf-2(lf)* mutant (Figure 6E, 6F, Figure 6-figure supplement 1 C).

362

363 Moreover, we found that the RNAi knockdown of *npp-6* suppresses the lifespan extension in the  
364 *lipl-4* *Tg* worms (Figure 6G, 6H) but does not affect the lifespan extension in the *daf-2(lf)*  
365 (Figure 6I, 6J) or the *isp-1(lf)* mutant (Figure 6-figure supplement 1 D, E). These results suggest  
366 that the nucleoporin protein NPP-6 is specifically involved in the regulation of lysosomal LIPL-

367 4-induced longevity. Given the importance of nucleoporin in nuclear transport, we further test  
368 whether nuclear import and/or export may play a role in regulating *lip1-4* *Tg* induced longevity.  
369 To this end, we knocked down *xpo-1* and *ima-3*, which encodes Exportin-1 and Importin- $\alpha$ ,  
370 mediating nuclear export and import, respectively, by RNAi. We found that the RNAi  
371 inactivation of *ima-3*, but not *xpo-1* suppresses the lifespan extension caused by *lip1-4* *Tg* (Figure  
372 6-figure supplement 1 F-H and Supplementary File 8). These results suggest that the increased  
373 proximity between lysosomes and the nucleus may facilitate the nuclear import of *lip1-4* *Tg*-  
374 induced lysosomal retrograde signals to promote longevity.

375

### 376 **Cystinosin positive mature lysosomes enrich specific lysosomal proteins**

377

378 The analysis of the candidates specifically detected in the *lip1-4* *Tg* worms suggests that the  
379 proportion of mature lysosomes may affect lysosomal protein composition. Although LMP-1 is a  
380 well-established lysosomal protein marker and highly abundant on the lysosomal surface, it can  
381 be also detected in late endosomes and sometimes in early endocytic compartments. With the  
382 hope to profile proteins enriched in mature lysosomes, we chose CTNS-1, the *C. elegans*  
383 lysosomal cystine transporter Cystinosin that is a well-established marker of mature lysosomes  
384 (Gahl et al., 1982; Jonas et al., 1982; Kalatzis et al., 2001). Using CRISPR knock-in lines with  
385 endogenous CTNS-1 and LMP-1 tagged with wrmScarlet and mNeonGreen, respectively, we  
386 found that CTNS-1 and LMP-1 signals show only partial overlap in the intestine, muscle,  
387 hypodermis and neurons (Figure 7-figure supplement 1). We then generated a transgenic strain  
388 expressing CTNS-1 tagged with both 3 $\times$ HA and RFP (CTNS-1 *lysoTg*). Fluorescence imaging of  
389 RFP confirmed the lysosomal localization of the CTNS-1 fusion protein in live organisms

390 (Figure 7A). Using this transgenic strain, we followed the same Lyso-IP and MS profiling  
391 pipeline. The correlation analysis shows good reproducibility among three independent  
392 biological replicates (Figure 7-figure supplement 2 A), and the PCA analysis indicates a clear  
393 separation between Lyso-IP samples and flow-through controls (Figure 7-figure supplement 2 B).  
394 Using the same selection criteria, we identified 293 candidates whose levels are enriched at least  
395 10-fold in the purified lysosomes than those in the flow-through controls among all independent  
396 biological replicates and show over 2-fold enrichment compared to the non-tag controls  
397 (Supplementary File 9). There are 95 lysosome-enriched proteins shared between the LMP-1 and  
398 the CTNS-1 Lyso-IP proteomic profiling datasets (Figure 7B, Supplementary File 9), and 47 of  
399 these shared proteins are annotated with lysosomal localization (Supplementary File 9). We have  
400 also crossed the CTNS-1 *lysotg* strain with the *lipl-4 Tg*, *daf-2(lf)*, and *glp-1(lf)* worms and then  
401 conducted Lyso-IP proteomic profiling. However, the pull-down efficiency was very low in  
402 these long-lived worms, which prevented us from identifying proteins unique to CTNS-1 Lyso-  
403 IP in those conditions.

404

405 In WT worms, the proportions of the identified proteins with different categories of subcellular  
406 annotation are comparable between LMP-1 and CTNS-1 Lyso-IP conditions (Figure 7C, 2E),  
407 and for proteins with lysosomal annotation, the proportion is 25% and 28% in LMP-1 and  
408 CTNS-1 Lyso-IP, respectively (Figure 7D). However, among the 121 proteins only identified in  
409 LMP-1 Lyso-IP, there are only 8 with lysosomal annotation (7%); while for the 198 proteins  
410 only identified in CTNS-1 Lyso-IP, 35 are with lysosomal annotation and the proportion remains  
411 as 18% (Figure 7D).

412

413 Among the lysosomal proteins that are unique to CTNS-1 Lyso-IP, there are autophagosome  
414 proteins and proteins that mediate the fusion between autophagosomes and lysosomes, including  
415 ATG-9/ATG9A (Popovic & Dikic, 2014), C33A11.2/DRAM2 (Crighton et al., 2006), EPG-  
416 7/RB1CC1 (Nishimura et al., 2013), and VAMP-7/VAMP8 (Diao et al., 2015; Itakura et al.,  
417 2012) (Figure 7E). Furthermore, the Ragulator complex components LMTR-2/3/5, the lysosomal  
418 amino acid transporter F13H10.3/SLC38A9 and the lysosomal calcium channel CUP-5/TRPML1  
419 that regulate mTORC1 signaling (Li et al., 2016; Rebsamen et al., 2015; Wang et al., 2015;  
420 Wyant et al., 2017) exhibited a higher enrichment in the lysosome purified from WT worms  
421 using CTNS-1 Lyso-IP than using LMP-1 Lyso-IP (Figure 7E). To further confirm the increased  
422 enrichment of mTORC1 signaling components with CTNS-1 lysosomes, we generated a  
423 CRISPR knock-in line with endogenous LMTR-3 tagged with wrmScarlet to visualize its  
424 subcellular localization. After crossing this line with LMP-1::mNeonGreen and CTNS-1::  
425 mNeonGreen knock-in lines, we found that LMTR-3 shows a complete overlap with CTNS-1 in  
426 the intestine, muscle and hypodermis (Figure 7F, Figure 7-figure supplement 2 C), but it only  
427 shows a partial overlap with LMP-1 in the intestine, muscle and hypodermis (Figure 7F, Figure  
428 7-figure supplement 2 D).

429  
430 Furthermore, when systematically examining 85 lysosome-related proteins that were previously  
431 annotated in *C. elegans* based on sequence homology (Sun et al., 2020), we found that 63 were  
432 detected in the proteomic profiling, while 22 were not detected likely due to their low abundance  
433 (Figure 7G). Many lysosomal hydrolases exhibit increased enrichments with CTNS-1 Lyso-IP.  
434 Interestingly, similar increased enrichments of these candidates were also observed in the LMP-1  
435 Lyso-IP result using the *lip1-4* Tg worms (Figure 7E, 7G). These results further support that the

436 long-lived *lip1-4* *Tg* worms carry more acidic lysosomes. The enrichment of cysteine proteases  
437 including CPR-6, LGMN-1, CPL-1, CPZ-1 and TAG-196 is consistent with that CTNS-1 is  
438 located at mature lysosomes as a cysteine transporter (Gahl et al., 1982; Jonas et al., 1982;  
439 Kalatzis et al., 2001). Together, we found that lysosome-enriched proteomes identified from both  
440 LMP-1 and CTNS-1 Lyso-IP consist of well-characterized lysosomal enzymes and integral  
441 membrane proteins as well as proteins that contribute to lysosomal signaling, dynamics and  
442 contact with other cellular compartments. Besides many known lysosomal proteins, various  
443 proteins that are not previously linked with lysosomes are now identified through these  
444 systematic analyses.

445

#### 446 **Lysosome-enriched proteins regulate different lysosomal activities**

447

448 To understand the role of these newly identified lysosome-enriched proteins in regulating  
449 lysosomal functions, we have examined their effects on lysosomes using an RNAi screen based  
450 on LysoSensor fluorescence intensity. We focused on 95 lysosome-enriched proteins shared  
451 between LMP-1 and CTNS-1 Lyso-IPs and knocked down their coding genes by RNAi, and then  
452 used LysoSensor probes to stain lysosomes. From screening these 95 candidates (Supplementary  
453 File 10), we have identified five genes whose inactivation cause changes in LysoSensor signal  
454 intensity, and four of them have human homologs, including two lysosomal v-ATPase subunits,  
455 UNC-32/ATP6V0A and VHA-5/ATP6V0A, the lysosomal amino acid transporter SLC-  
456 36.2/SLC36A1 (SLC36A4), and a transmembrane protein R144.6/TMEM144 (Supplementary  
457 File 10, Figure 8A-E, Figure 8-figure supplement 1). We further examined their effects on the  
458 lysosomal number, size, and pH. We found that the RNAi knockdown of the two lysosomal v-

459 ATPase subunits, UNC-32 and VHA-5, lead to decreased lysosomal numbers (Figure 8F), but an  
460 increase in the lysosomal size (Figure 8G). We also used fluorescence lifetime microscopy to  
461 measure the fluorescence lifetime of LysoSensor, which is negatively correlated with pH (Deng  
462 et al., 2023; Lin et al., 2001). Unexpectedly, we found that the RNAi knockdown of *unc-32*  
463 increases the fluorescence lifetime of LysoSensor, indicating a decrease in lysosomal pH (Figure  
464 8H). We think this decrease is an attempt to compensate for the 2.5-fold reduction in the total  
465 number of lysosomes. Overall, *unc-32* inactivation compromises lysosomal v-ATPase and leads  
466 to a defect in lysosomal maturation. On the other hand, the RNAi knockdown of R144.6 did not  
467 affect lysosomal number or size but increased lysosomal pH (Figure 8F-H).

468

469 Unlike well-known lysosomal proteins, UNC-32, VHA-5 and SLC-36.2, the subcellular  
470 localization of the R144.6 protein remains unknown. R144.6 is a predicted carbohydrate  
471 transporter, and structural simulation using AlphaFold2 suggested it as a solute carrier family  
472 (SLC) transporter (Figure 8I). We generated a CRISPR knock-in line in which the endogenous  
473 R144.6 protein is fused with mNeonGreen and then stained these worms with LysoTracker Red  
474 to mark lysosomes. In the hypodermis, we found that mNeonGreen and LysoTracker Red signals  
475 overlap, confirming the lysosomal localization of this newly identified transmembrane protein  
476 from Lyso-IP (Figure 8J). On the other hand, its expression was not detected in the muscle, and  
477 in the intestine, its mNeonGreen signals did not overlap with LysoTracker Red, which is  
478 consistent with tissue-specific Lyso-IP analyses. R144.6 was enriched in the hypodermis-specific  
479 Lyso-IP at a similar level as in the whole-body Lyso-IP; however, it was not detected in the  
480 muscle- or intestine-specific Lyso-IP. These results further support the enrichment specificity of

481 proteins at the lysosome in different tissues as well as the power of the Lyso-IP proteomic  
482 profiling in discovering new lysosomal proteins with functional significance.

483

484 **DISCUSSION**

485

486 Our studies reveal the heterogeneity of lysosomal protein composition that is associated with  
487 lysosomal status, tissue specificity, and organism longevity. Through systematic profiling of  
488 lysosome-enriched proteins under different conditions, we confirmed the induction of lysosome-  
489 related autophagy by different longevity-promoting pathways, unveiled increased cellular  
490 interaction between lysosomes and the nucleus upon the induction of lysosomal lipolysis and its  
491 contribution to longevity regulation, and underlined the importance of the spatial control of  
492 AMPK activation in regulating longevity. Our work provides not only methods for future studies  
493 to profile the dynamics of the lysosomal proteome in response to diverse physiological inputs,  
494 but also resources for understanding the vital contribution of these dynamics in modulating  
495 signal transduction, organelle crosstalk and organism longevity.

496

497 These proteomic studies can provide hits for changes in the interaction between lysosomes and  
498 other organelles under different conditions. One example is the lysosome-nucleus interaction. In  
499 the Lyso-IP fraction from WT worms, we did not detect any proteins with sole nuclear  
500 localization; however, in the Lyso-IP fraction from the *lipl-4 Tg* or *daf-2(lf)* mutant worms,  
501 nuclear proteins were identified and the percentage of the increase over WT is significantly  
502 higher in the *lipl-4 Tg* worms ( $p<0.05$ , Figure 6A, Figure 6-figure supplement 1 I). Based on this  
503 finding, we discovered the previously unknown perinuclear accumulation of lysosomes in the

504 *lipl-4* *Tg* worms (Figure 6C, 6D) and further confirmed its importance for longevity regulation  
505 (Figure 6G, 6H). It has been shown previously that perinuclear lysosomes are more acidic than  
506 peripheral lysosomes (Johnson et al., 2016; Webb et al., 2021). Thus, the increase in perinuclear  
507 lysosomes may be associated with the increased proportion of mature lysosomes in the *lipl-4* *Tg*  
508 worms, which is supported by the increased enrichments of lysosomal v-ATPase,  
509 channels/transporters and hydrolases (Figure 5A). This increased distribution of lysosomes  
510 toward the perinuclear region could facilitate proteins and metabolites transporting from the  
511 lysosome to the nucleus through the nuclear pore and in turn their signaling effects. However,  
512 whether this perinuclear distribution of lysosomes is associated with an increase in the direct  
513 contact between lysosomes and the nucleus remains to be determined using technologies with  
514 higher spatial resolution such as electron microscopy imaging. On the other hand, we did not  
515 detect perinuclear accumulation of lysosomes in the *daf-2(lf)* mutant worms by cellular imaging,  
516 and the nuclear proteins detected through LMP-1 Lyso-IP from the *daf-2(lf)* mutant worms are  
517 mainly involved in RNA splicing. In yeast cells, defects in pre-mRNA processing have been  
518 associated with nucleophagy (Leger-Silvestre et al., 2005) that involves SQSTM1 and lysosomes  
519 (Ivanov et al., 2013; Mijaljica & Devenish, 2013). We thus speculate that the increased  
520 enrichment of nuclear proteins in the *daf-2(lf)* mutant worms may be associated with the  
521 induction of nucleophagy but not changes in lysosomal positioning.

522

523 mTORC1 and AMPK are key metabolic checkpoints that regulate anabolic and catabolic  
524 processes in mutually opposing ways. In sensing the lack of nutrients, AMPK signals activate the  
525 catabolic process while inhibiting the anabolic one. On the other hand, responding to nutrient  
526 availability, mTORC1 activation upregulates anabolic metabolism and promotes cell growth.

527 Intriguingly, it is now known that both mTORC1 and AMPK are recruited to the lysosomal  
528 surface for activation, which requires the scaffold Ragulator complex that consists of LAMTOR  
529 subunits. We found that the Ragulator complex (LMTR-2, 3 and 5) shows a higher enrichment in  
530 the lysosome purified from WT worms using CTNS-1 Lyso-IP than using LMP-1 Lyso-IP  
531 (Figure 7E), and cellular imaging of endogenous LMTR-3 confirmed its much higher overlap  
532 with CTNS-1-positive lysosomes than with LMP-1-positive lysosomes (Figure 7F, Figure 7-  
533 figure supplement 2 C, D). These results suggest a predominant association of the Ragulator  
534 complex with mature lysosomes, which could in turn determine the preference of mTORC1 and  
535 AMPK activation at the lysosomal surface. Alternatively, it would be also possible that the  
536 Ragulator complex carries a preference toward CTNS-1/Cystinosin-containing lysosomes, which  
537 would infer the interaction between lysosomal cysteine metabolism and mTORC1 signaling.  
538 Interestingly, previous studies show that Cystinosin co-immunoprecipitates with the Ragulator  
539 complex in mammalian cells (Andrzejewska et al., 2016), and in *Drosophila*, cysteine efflux  
540 from the lysosome via Cystinosin antagonizes mTORC1 signaling and upregulates the  
541 tricarboxylic acid cycle (Jouandin et al., 2022). Whether this inhibitory effect of lysosomal  
542 cysteine on mTORC1 is related to the preferential interaction between the Ragulator complex  
543 and Cystinosin would be an interesting question for future studies.

544

545 Both mTORC1 and AMPK have been implicated in the regulation of longevity across different  
546 species, being intertwined with other longevity regulatory mechanisms (Savini et al., 2019). In  
547 the long-lived *lipl-4* *Tg* worms, the lysosomal enrichment of the Ragulator complex is increased  
548 with LMP-1 Lyso-IP, which may be a result of the increased proportion of mature lysosomes  
549 upon the induction of lysosomal lipolysis. At the same time, we could not rule out the possibility

550 that the increased enrichment of the Ragulator complex is a result of the induced level of  
551 lysosomal CTNS-1/Cystinosin in the *lipl-4* *Tg* worms. We found that with LMP-1 Lyso-IP, the  
552 level of the CTNS-1/Cystinosin transporter is increased in the *lipl-4* *Tg* worms, together with the  
553 increase of several cysteine cathepsins (Figure 7G). Our previous studies found that  
554 mitochondrial  $\beta$ -oxidation is increased in the *lipl-4* *Tg* worms, leading to decreased triglyceride  
555 storage (Ramachandran et al., 2019). The *lipl-4* *Tg* worms also show induced autophagy (Mak et  
556 al., 2020). These phenotypes are the same as those observed in fruit flies with Cystinosin  
557 overexpression (Jouandin et al., 2022). Considering the inhibitory effect of Cystinosin on  
558 mTORC1 in fruit flies, the induction of Cystinosin in the *lipl-4* *Tg* worms might reduce  
559 mTORC1 signaling. In supporting this idea, our unpublished study shows that *lipl-4* *Tg* does not  
560 further enhance the lifespan extension of the *raga-1* mutant that has reduced mTORC1 signaling.  
561 Furthermore, our study reveals the lysosomal enrichment of AMPK in the *lipl-4* *Tg* worms, and  
562 its requirement for the longevity effect (Figure 5B, 5C). On the other hand, the involvement of  
563 lysosomal mTORC1 and AMPK signaling in regulating the longevity effect was not identified in  
564 the *daf-2(lf)*, *isp-1(lf)* or *glp-1(lf)* mutant. Organelle-specific signaling regulation of longevity  
565 would be interesting topics for future studies.

566

## 567 MATERIALS AND METHODS

568

### 569 *C. elegans* strains and maintenance

570 The following strains were used in this study: N2, CB1370 *daf-2(e1370)*, RB754 *aak-2(ok524)*,  
571 *unc-76(e911)*, MCW953 *nre-1(hd20);lin-15b(hd126)*, MCW14 *raxIs3 [ges-1p::lipl-4::SL2GFP]*,  
572 MCW859 *raxIs103[sur-5p:lmp-1::RFP-3×HA;unc-76(+)]* (*sur-5* promoter for whole-body

573 overexpression), MCW935 *daf-2(e1370);raxIs103[sur-5p:lmp-1::RFP-3×HA;unc-76(+)]*,  
574 MCW923 *raxIs3[ges-1p::lipl-4::SL2GFP];raxIs103[sur-5p:lmp-1::RFP-3×HA;unc-76(+)]*,  
575 MCW861 *unc-76(e911);raxEx311[Pmyo-3:lmp-1::RFP-3×HA;unc-76(+)]* (myo-3 promoter for  
576 muscle overexpression), MCW924 *unc-76(e911); raxEx346[Pcol-12:lmp-1::RFP-3×HA;unc-*  
577 *76(+)]* (col-12 promoter for hypodermis overexpression), MCW862 *unc-*  
578 *76(e911);raxEx312[Punc-119:lmp-1::RFP-3×HA;unc-76(+)]* (unc-119 promoter for neuron  
579 overexpression), MCW914 *unc-76(e911);raxEx341[Pges-1:lmp-1::RFP-3×HA;unc-76(+)]*  
580 (*ges-1* promoter for intestine overexpression), MCW934 *raxIs118[sur-5p:ctns-1::RFP-*  
581 *3×HA;unc-76(+)]*. The strains *Y58A7A.1(syb7950[Y58A7A.1::mNeonGreen])*,  
582 *R144.6(syb4893[R144.6::mNeonGreen], lmp-1(syb4827[lmp-1::mNeonGreen]), ctns-*  
583 *1(syb5019[ctns-1::wrmscarlet]), ctns-1(syb4805[ctns-1::mNeonGreen]), and lmtr-*  
584 *3(syb8005[wrmscarlet::lmtr-3])* were generated via CRISPR/Cas9 genome editing by  
585 SunyBiotech (Fuzhou, China). The strains N2, CB1370, and RB754 were obtained from  
586 *Caenorhabditis* Genetics Center (CGC). The strain *unc-76(e911)* was obtained from Dr. Zheng  
587 Zhou's Lab. Other strains were generated in our lab.

588

589 *C. elegans* strains were maintained at 20°C on standard NGM agar plates seeded with OP50  
590 *E.coli* (HT115 *E. coli* for RNAi experiments) using standard protocols (Stiernagle, 2006) and  
591 kept at least three generations without starvation before experiments.

592

### 593 **Molecular cloning and generating transgenics**

594 All the expression constructs were generated using the Multisite Gateway System (Invitrogen) as  
595 previously described (Mutlu et al., 2020). The *lmp-1* and *ctns-1* coding sequences were PCR-

596 amplified from *C. elegans* cDNA then inframe fused with RFP-3×HA, and all promoters were  
597 PCR-amplified from *C. elegans* genomic DNA.

598

599 Transgenic strains were generated by microinjecting the day-1-adult germline of *unc-76(e911)*  
600 worms with DNA mixture containing expression construct and *unc-76(+)* rescuing plasmid. For  
601 integration strains, the stable extrachromosomal arrays were integrated with gamma irradiation  
602 (4500 rads for 5.9 minutes) and backcrossing to wild-type N2 at least 8 times.

603

#### 604 **Lysosome immunoprecipitation (Lyo-IP)**

605 Lyso-IP is based on the method used in mammalian cells (Abu-Remaileh et al., 2017). Briefly,  
606 transgenic strains stably expressing C-terminal RFP- and 3×HA-tagged lysosomal membrane  
607 protein LMP-1 or CTNS-1 under whole-body *Psur-5* or tissue-specific promoters were generated.  
608 Around 160,000 day-1-adult worms per genotype were collected, washed 3 times with M9 buffer  
609 then washed 1 time with ice-cold KPBS buffer (136 mM KCl, 10 mM KH<sub>2</sub>PO<sub>4</sub>). Worms in 2 ml  
610 ice-cold KPBS were quickly homogenized with Dounce homogenizer (Sigma cat. # D9063) on  
611 ice until no visible animals were seen under the microscope. The lysate was centrifuged at 1000  
612 g for 3 min at 4 °C to remove debris and then the supernatant was incubated with anti-HA  
613 magnetic beads (Thermo Fisher Scientific, cat. # 88837, washed 3 times with ice-cold KPBS  
614 buffer before use. Each IP needs a 160 ul of beads.) for 6 minutes at 20 °C with rotation. The  
615 bound beads and flowthrough were separated using a magnetic stand. The bound bead fraction  
616 was washed 4 times with ice-cold KPBS. The bound bead and flowthrough fractions were both  
617 used for LC/MS-based proteomics analyses. In order to finish processing all samples as quickly  
618 as possible, no more than 3 samples were processed in parallel.

619

620 **LC/MS-based proteomic analyses**

621 The bound beads after washing were directly eluted in 100  $\mu$ l of 5% SDS buffer and trypsin  
622 digestion was carried out using S-Trap<sup>TM</sup> (Protifi, NY) as per manufacturer's protocol. For the  
623 flow-through sample after IP, 100  $\mu$ l sample was diluted in 5% SDS buffer and trypsin digestion  
624 was carried out using S-Trap<sup>TM</sup>. The peptide concentration was measured using the Pierce<sup>TM</sup>  
625 Quantitative Colorimetric Peptide Assay (Thermo Scientific cat. # 23275). The digested peptides  
626 were subjected to simple C18 clean-up using a C18 disk plug (3M Empore C18) and dried in a  
627 speed vac. 1  $\mu$ g of the peptide was used for LC-MS/MS analysis which was carried out using a  
628 nano-LC 1200 system (Thermo Fisher Scientific, San Jose, CA) coupled to Orbitrap Fusion<sup>TM</sup>  
629 Lumos ETD mass spectrometer (Thermo Fisher Scientific, San Jose, CA). The peptides were  
630 loaded on a two-column setup using a pre-column trap of 2 cm  $\times$  100  $\mu$ m size (Reprosil-Pur  
631 Basic C18 1.9  $\mu$ m, Dr. Maisch GmbH, Germany) and a 5 cm  $\times$  75  $\mu$ m analytical column  
632 (Reprosil-Pur Basic C18 1.9  $\mu$ m, Dr. Maisch GmbH, Germany) with a 75 min gradient of 5-28%  
633 acetonitrile/0.1% formic acid at a flow rate of 750 nl/min. The eluted peptides were directly  
634 electro-sprayed into a mass spectrometer operated in the data-dependent acquisition (DDA)  
635 mode. The full MS scan was acquired in Orbitrap in the range of 300-1400 m/z at 120,000  
636 resolution followed by top 30 MS2 in Ion Trap (AGC 5000, MaxIT 35 ms, HCD 28% collision  
637 energy) with 15 sec dynamic exclusion time.

638

639 The raw files were searched using the Mascot algorithm (Mascot 2.4, Matrix Science) against the  
640 *Caenorhabditis elegans* NCBI refseq protein database in the Proteome Discoverer (PD 2.1,  
641 Thermo Fisher) interface. The precursor mass tolerance was set to 20 ppm, fragment mass

642 tolerance to 0.5 Da, maximum of two missed cleavage was allowed. Dynamic modification of  
643 oxidation on methionine, protein N-terminal Acetylation and deamidation (N/Q) was allowed.  
644 Assigned peptides are filtered with a 1% FDR using Percolator validation based on q-value, and  
645 the Peptide Spectrum Matches (PSMs) output from PD2.5 will be used to group peptides onto  
646 gene levels using the ‘gpGrouper’ algorithm (Saltzman et al., 2018). This in-house program uses  
647 a universal peptide grouping logic to accurately allocate and provide MS1 based quantification  
648 across multiple gene products. Gene-protein products (GPs) quantification will be performed  
649 using the label-free, intensity-based absolute quantification (iBAQ). iBAQ-based fraction of total  
650 values (iFOT) was calculated by dividing the iBAQ for each gene product by the total species  
651 iBAQ to normalize sample amount variation.

652

### 653 **Antibodies**

654 Anti-*C. elegans* LMP-1, HSP-60, CYP-33, and SVQ-8 monoclonal antibodies were purchased  
655 from Developmental Studies Hybridoma Bank (DSHB). Those antibodies were originally  
656 generated by Dr. Michael L. Nonet’s lab (Hadwiger et al., 2010). Anti-β-actin antibody (C4) was  
657 purchased from Santa Cruz (sc-47778).

658

### 659 **Microscopy imaging**

#### 660 Regular microscopy

661 Tissue-specific lyso-tag expression example images (Figure 3A) were captured using Leica  
662 DMi8 THUNDER Imaging Systems using 20× objective. The images that show the  
663 colocalization between CRISPR knock-in lines LMP-1::mNeonGreen and CTNS-1::wrnScarlet  
664 were captured by Zeiss LSM 980 with Airyscan. The images that show the colocalization

665 between wrmScarlet::LMTR-3 and LMP-1::mNeonGreen/CTNS-1::mNeonGreen were taken  
666 using Nikon CSU-W1 spinning disk confocal microscopy system. Other microscopy images  
667 were captured using an Olympus FV3000 confocal microscopy system using 60× or 20×  
668 objective. *C. elegans* were anesthetized in 1% sodium azide in M9 buffer and placed on a 2%  
669 agarose pad sandwiched between the glass microscopic slide and coverslip.

670

671 **Fluorescence lifetime microscopy**

672 L1 RNAi sensitive *nre-1(hd20);lin-15b(hd126)* worms were seeded on 3.5cm RNAi plates and  
673 raised at 20°C for two days, and then around 20 worms each well were transferred to the 3.5cm  
674 RNAi plates containing RNAi bacteria and 0.5 µM of LysoSensor Green DND-189  
675 (Invitrogen™ L7535) and raised for 18h (in dark) at 20°C. The worms were imaged using ISS  
676 Q2 Time-resolved Laser Scanning Confocal Nanoscope. The laser excitation wavelength was set  
677 at 476nm and the 500-633nm emission filter was used to detect the LysoSensor Green signal. The  
678 first pair of intestinal cells of each worm was imaged. The lifetimes of LysoSensor-containing  
679 puncta were measured using ISS VistaVision software. The pH of the lysosome was then  
680 calculated based on the LysoSensor lifetime-pH calibration curve (Deng et al., 2023).

681

682 **LysoSensor RNAi screen**

683 The primary screen was performed on 95 lysosomal-enriched candidates shared between the  
684 LMP-1 and the CTNS-1 Lyso-IP proteomic profiling datasets. Each RNAi bacteria clone was  
685 seeded onto 12-well RNAi plates containing 1 mM IPTG and allowed to dry. The dried plates  
686 were then incubated at room temperature overnight to induce dsRNA expression. Synchronized  
687 L1 *nre-1(hd20);lin-15b(hd126)* worms were seeded on 12-well RNAi plates and raised at 20 °C

688 for two days, and then around 30 worms each well were transferred to the RNAi plates  
689 containing RNAi bacteria and 0.5  $\mu$ M of LysoSensor Green DND-189. After 18 hours,  
690 LysoSensor signals were examined by the naked eyes using a Nikon SMZ18 fluorescence stereo  
691 microscope. The candidates with obvious LysoSensor alteration were selected for the secondary  
692 LysosSensor RNAi screen. In the secondary screen, worms stained using LysoSensor Green  
693 DND-189 were imaged by the Olympus FV3000 confocal microscopy system. The changes in  
694 LysoSensor signals in the first pair of intestine cells were quantified by ImageJ (including  
695 intensity, size, and number).

696

### 697 **Lysosome distribution quantification**

698 The quantification method was modified from previous publications on lysosomal distribution in  
699 mammalian cell lines (Johnson et al., 2016; Willett et al., 2017). Images were first captured using  
700 Olympus Fluoview software and imported into Matlab by the Bio-Formats tool (Linkert et al.,  
701 2010). Next, the cell membrane and nuclear membrane are outlined manually. The algorithm  
702 (code included in Supplementary materials) determines the geometric center of the nucleus and  
703 radiates at all angles to locate line segments between the nuclear and cell membrane. The line  
704 segments are then evenly divided and circled to segment the cytosol into different regions. We  
705 calculate: 1. The mean RFP fluorescence distribution across regions (normalized to the mean  
706 intensity of the whole cell to avoid variations of RFP expression across cells) (Figure 6D, 6F); 2.  
707 The cumulative intensity distribution from the most perinuclear region to the most peripheral  
708 region (normalized to the overall intensity of the whole cell) (Figure 6-figure supplement 1 B, C).  
709 The algorithm requires a convex shape of the cell, and most of the gut cells imaged meet this  
710 need.

711

712 **Lifespan assays**

713 Worms were synchronized by bleach-based egg preparation and subsequent starvation in M9  
714 buffer for over 24 hours. Synchronized L1 worms were placed on the plates, and animals were  
715 synchronized again by manual picking at mid L4 stage and marked as Day 0. Approximately 90-  
716 120 worms were placed in three parallel plates for each condition. Worms are hence observed  
717 and transferred to freshly made RNAi plates every other day. Animals are categorized as alive,  
718 dead (cessation of movement in response to platinum wire probing) or censored. The statistical  
719 analyses were performed with the SPSS23 Kaplan-Meier survival function and the log-rank test.  
720 GraphPad Prism 9 was used to graph the results.

721

722 **Structural stimulation by AlphaFold2**

723 The structure of R144.6 (UniProt: Q10000) was predicted by AlphaFold2 and downloaded from  
724 The AlphaFold Protein Structure Database (<https://alphafold.ebi.ac.uk/>) (Jumper et al., 2021;  
725 Varadi et al., 2022). The molecular graphics of the R144.6 structure were performed with UCSF  
726 Chimera (Pettersen et al., 2004).

727

728 **Statistical methods**

729 Principal components analysis (PCA) was performed by R package Factextra (Le et al., 2008)  
730 with the normalized iFOT abundance of proteins detected as the input. The Pearson correlation  
731 matrices and coefficient (r) among replicates were generated by GraphPad Prism 9. The unpaired,  
732 two-tailed t-tests for the multiple comparisons were used to calculate the p-values in the  
733 correlation analyses by GraphPad Prism 9.

734

735 **Data availability**

736 The mass spectrometry data for protein identification have been deposited via the MASSIVE

737 repository (MSV000090909) to the Proteome X change Consortium

738 (<http://proteomecentral.proteomexchange.org>) with the dataset identifier PXD038865.

739 Analysis code for Figure 6D, 6F and Figure 6-figure supplement 1 is included in the Source

740 Code File 1.

741

742 **Conflict of Interest**

743 None declared.

744

745 **ACKNOWLEDGEMENTS**

746 We thank A. Dervisefendic and P. Svay for maintenance support; Mass Spectrometry Proteomics

747 Core of Baylor College of Medicine for mass spectrometry proteomic analysis; Z. Zhou (Baylor

748 College of Medicine) for sharing *unc-76(e911)* strain. Some strains were obtained from the

749 *Caenorhabditis* Genetics Center (CGC), which is funded by the NIH Office of Research

750 Infrastructure Programs (P40 OD010440). M.C.W. is currently supported by Howard Hughes

751 Medical Institute, and Y.Y. is currently supported by the National Natural Science Foundation of

752 China 32071146.

753

754 **REFERENCE**

755

756 Abu-Remaileh, M., Wyant, G. A., Kim, C., Laqtom, N. N., Abbasi, M., Chan, S. H., Freinkman, E.,  
757 & Sabatini, D. M. (2017). Lysosomal metabolomics reveals V-ATPase- and mTOR-

758 dependent regulation of amino acid efflux from lysosomes. *Science*, 358(6364), 807-813.  
759 <https://doi.org/10.1126/science.aan6298>

760 Andrzejewska, Z., Nevo, N., Thomas, L., Chhuon, C., Bailleux, A., Chauvet, V., Courtoy, P. J., Chol,  
761 M., Guerrera, I. C., & Antignac, C. (2016). Cystinosin is a Component of the Vacuolar H+-  
762 ATPase-Ragulator-Rag Complex Controlling Mammalian Target of Rapamycin Complex 1  
763 Signaling. *J Am Soc Nephrol*, 27(6), 1678-1688.  
764 <https://doi.org/10.1681/ASN.2014090937>

765 Apfeld, J., O'Connor, G., McDonagh, T., DiStefano, P. S., & Curtis, R. (2004). The AMP-activated  
766 protein kinase AAK-2 links energy levels and insulin-like signals to lifespan in *C. elegans*.  
767 *Genes Dev*, 18(24), 3004-3009. <https://doi.org/10.1101/gad.1255404>

768 Appelqvist, H., Waster, P., Kagedal, K., & Ollinger, K. (2013). The lysosome: from waste bag to  
769 potential therapeutic target. *J Mol Cell Biol*, 5(4), 214-226.  
770 <https://doi.org/10.1093/imcb/mjt022>

771 Ballabio, A., & Bonifacino, J. S. (2020). Lysosomes as dynamic regulators of cell and organismal  
772 homeostasis. *Nature reviews Molecular cell biology*, 21(2), 101-118.  
773 <https://doi.org/10.1038/s41580-019-0185-4>

774 Ballabio, A., & Gieselmann, V. (2009). Lysosomal disorders: from storage to cellular damage.  
775 *Biochim Biophys Acta*, 1793(4), 684-696. <https://doi.org/10.1016/j.bbamcr.2008.12.001>

776 Berman, J. R., & Kenyon, C. (2006). Germ-cell loss extends *C. elegans* life span through  
777 regulation of DAF-16 by kri-1 and lipophilic-hormone signaling. *Cell*, 124(5), 1055-1068.  
778 <https://doi.org/10.1016/j.cell.2006.01.039>

779 Braulke, T., & Bonifacino, J. S. (2009). Sorting of lysosomal proteins. *Biochimica Et Biophysica  
780 Acta-Molecular Cell Research*, 1793(4), 605-614.  
781 <https://doi.org/10.1016/j.bbamcr.2008.10.016>

782 Brown, C. A., & Black, S. D. (1989). Membrane topology of mammalian cytochromes P-450 from  
783 liver endoplasmic reticulum. Determination by trypsinolysis of phenobarbital-treated  
784 microsomes. *J Biol Chem*, 264(8), 4442-4449.  
785 <https://www.ncbi.nlm.nih.gov/pubmed/2925650>

786 Castellano, B. M., Thelen, A. M., Moldavski, O., Feltes, M., van der Welle, R. E., Mydock-  
787 McGrane, L., Jiang, X., van Eijkeren, R. J., Davis, O. B., Louie, S. M., Perera, R. M., Covey,  
788 D. F., Nomura, D. K., Ory, D. S., & Zoncu, R. (2017). Lysosomal cholesterol activates  
789 mTORC1 via an SLC38A9-Niemann-Pick C1 signaling complex. *Science*, 355(6331), 1306-  
790 1311. <https://doi.org/10.1126/science.aag1417>

791 Crighton, D., Wilkinson, S., O'Prey, J., Syed, N., Smith, P., Harrison, P. R., Gasco, M., Garrone, O.,  
792 Crook, T., & Ryan, K. M. (2006). DRAM, a p53-induced modulator of autophagy, is critical  
793 for apoptosis. *Cell*, 126(1), 121-134. <https://doi.org/10.1016/j.cell.2006.05.034>

794 Cruciat, C. M., Ohkawara, B., Acebron, S. P., Karaulanov, E., Reinhard, C., Ingelfinger, D., Boutros,  
795 M., & Niehrs, C. (2010). Requirement of prorenin receptor and vacuolar H+-ATPase-  
796 mediated acidification for Wnt signaling. *Science*, 327(5964), 459-463.  
797 <https://doi.org/10.1126/science.1179802>

798 Davidson, S. M., & Vander Heiden, M. G. (2017). Critical Functions of the Lysosome in Cancer  
799 Biology. *Annu Rev Pharmacol Toxicol*, 57, 481-507. <https://doi.org/10.1146/annurev-pharmtox-010715-103101>

801 de Araujo, M. E. G., Naschberger, A., Furnrohr, B. G., Stasyk, T., Dunzendorfer-Matt, T., Lechner,  
802 S., Welti, S., Kremser, L., Shivalingaiah, G., Offterdinger, M., Lindner, H. H., Huber, L. A.,  
803 & Scheffzek, K. (2017). Crystal structure of the human lysosomal mTORC1 scaffold  
804 complex and its impact on signaling. *Science*, 358(6361), 377-381.  
805 <https://doi.org/10.1126/science.aao1583>

806 De Franceschi, N., Hamidi, H., Alanko, J., Sahgal, P., & Ivaska, J. (2015). Integrin traffic - the  
807 update. *J Cell Sci*, 128(5), 839-852. <https://doi.org/10.1242/jcs.161653>

808 Deng, D., Guan, Y., Wang, B., Zheng, H., Mutlu, A. S., & Wang, M. C. (2023). Quantitative  
809 Profiling of Lysosomal pH Heterogeneity using Fluorescence Lifetime Imaging  
810 Microscopy. *bioRxiv*, 2023.2009.2025.559395.  
811 <https://doi.org/10.1101/2023.09.25.559395>

812 Diao, J., Liu, R., Rong, Y., Zhao, M., Zhang, J., Lai, Y., Zhou, Q., Wilz, L. M., Li, J., Vivona, S.,  
813 Pfuetzner, R. A., Brunger, A. T., & Zhong, Q. (2015). ATG14 promotes membrane  
814 tethering and fusion of autophagosomes to endolysosomes. *Nature*, 520(7548), 563-566.  
815 <https://doi.org/10.1038/nature14147>

816 Eapen, V. V., Swarup, S., Hoyer, M. J., Paulo, J. A., & Harper, J. W. (2021). Quantitative  
817 proteomics reveals the selectivity of ubiquitin-binding autophagy receptors in the  
818 turnover of damaged lysosomes by lysophagy. *eLife*, 10.  
819 <https://doi.org/10.7554/eLife.72328>

820 Eskelinen, E. L. (2006). Roles of LAMP-1 and LAMP-2 in lysosome biogenesis and autophagy.  
821 *Mol Aspects Med*, 27(5-6), 495-502. <https://doi.org/10.1016/j.mam.2006.08.005>

822 Ewan, L. C., Jopling, H. M., Jia, H. Y., Mittar, S., Bagherzadeh, A., Howell, G. J., Walker, J. H.,  
823 Zachary, I. C., & Ponnambalam, S. (2006). Intrinsic tyrosine kinase activity is required for  
824 vascular endothelial growth factor receptor 2 ubiquitination, sorting and degradation in  
825 endothelial cells. *Traffic*, 7(9), 1270-1282. <https://doi.org/10.1111/j.1600-0854.2006.00462.x>

826 Fehrenbacher, N., & Jaattela, M. (2005). Lysosomes as targets for cancer therapy. *Cancer Res*,  
827 65(8), 2993-2995. <https://doi.org/10.1158/0008-5472.CAN-05-0476>

828 Feng, J., Bussiere, F., & Hekimi, S. (2001). Mitochondrial electron transport is a key determinant  
829 of life span in *Caenorhabditis elegans*. *Dev Cell*, 1(5), 633-644.  
830 [https://doi.org/10.1016/s1534-5807\(01\)00071-5](https://doi.org/10.1016/s1534-5807(01)00071-5)

831 Folick, A., Oakley, H. D., Yu, Y., Armstrong, E. H., Kumari, M., Sanor, L., Moore, D. D., Ortlund, E.  
832 A., Zechner, R., & Wang, M. C. (2015). Lysosomal signaling molecules regulate longevity  
833 in *Caenorhabditis elegans*. *Science*, 347(6217), 83-86.  
834 <https://doi.org/10.1126/science.1258857>

835 Forgac, M. (2007). Vacuolar ATPases: rotary proton pumps in physiology and pathophysiology.  
836 *Nat Rev Mol Cell Biol*, 8(11), 917-929. <https://doi.org/10.1038/nrm2272>

837 Gahl, W. A., Bashan, N., Tietze, F., Bernardini, I., & Schulman, J. D. (1982). Cystine transport is  
838 defective in isolated leukocyte lysosomes from patients with cystinosis. *Science*,  
839 217(4566), 1263-1265. <https://doi.org/10.1126/science.7112129>

840 Gallet, A., & Therond, P. P. (2005). Temporal modulation of the Hedgehog morphogen gradient  
841 by a patched-dependent targeting to lysosomal compartment. *Developmental Biology*,  
842 277(1), 51-62. <https://doi.org/10.1016/j.ydbio.2004.09.005>

844 Gao, Y., Chen, Y., Zhan, S., Zhang, W., Xiong, F., & Ge, W. (2017). Comprehensive proteome  
845 analysis of lysosomes reveals the diverse function of macrophages in immune responses.  
846 *Oncotarget*, 8(5), 7420-7440. <https://doi.org/10.18632/oncotarget.14558>

847 Grant, B., & Hirsh, D. (1999). Receptor-mediated endocytosis in the *Caenorhabditis elegans*  
848 oocyte. *Mol Biol Cell*, 10(12), 4311-4326. <https://doi.org/10.1091/mbc.10.12.4311>

849 Graves, A. R., Curran, P. K., Smith, C. L., & Mindell, J. A. (2008). The Cl<sup>-</sup>/H<sup>+</sup> antiporter ClC-7 is the  
850 primary chloride permeation pathway in lysosomes. *Nature*, 453(7196), 788-792.  
851 <https://doi.org/10.1038/nature06907>

852 Hadwiger, G., Dour, S., Arur, S., Fox, P., & Nonet, M. L. (2010). A monoclonal antibody toolkit for  
853 *C. elegans*. *PLoS One*, 5(4), e10161. <https://doi.org/10.1371/journal.pone.0010161>

854 Hansen, M., Rubinsztein, D. C., & Walker, D. W. (2018). Autophagy as a promoter of longevity:  
855 insights from model organisms. *Nat Rev Mol Cell Biol*, 19(9), 579-593.  
856 <https://doi.org/10.1038/s41580-018-0033-y>

857 Hartl, F. U., Martin, J., & Neupert, W. (1992). Protein folding in the cell: the role of molecular  
858 chaperones Hsp70 and Hsp60. *Annu Rev Biophys Biomol Struct*, 21, 293-322.  
859 <https://doi.org/10.1146/annurev.bb.21.060192.001453>

860 Itakura, E., Kishi-Itakura, C., & Mizushima, N. (2012). The hairpin-type tail-anchored SNARE  
861 syntaxin 17 targets to autophagosomes for fusion with endosomes/lysosomes. *Cell*,  
862 151(6), 1256-1269. <https://doi.org/10.1016/j.cell.2012.11.001>

863 Ivanov, A., Pawlikowski, J., Manoharan, I., van Tuyn, J., Nelson, D. M., Rai, T. S., Shah, P. P.,  
864 Hewitt, G., Korolchuk, V. I., Passos, J. F., Wu, H., Berger, S. L., & Adams, P. D. (2013).  
865 Lysosome-mediated processing of chromatin in senescence. *J Cell Biol*, 202(1), 129-143.  
866 <https://doi.org/10.1083/jcb.201212110>

867 Johnson, D. E., Ostrowski, P., Jaumouille, V., & Grinstein, S. (2016). The position of lysosomes  
868 within the cell determines their luminal pH. *J Cell Biol*, 212(6), 677-692.  
869 <https://doi.org/10.1083/jcb.201507112>

870 Jonas, A. J., Greene, A. A., Smith, M. L., & Schneider, J. A. (1982). Cystine accumulation and loss  
871 in normal, heterozygous, and cystinotic fibroblasts. *Proc Natl Acad Sci U S A*, 79(14),  
872 4442-4445. <https://doi.org/10.1073/pnas.79.14.4442>

873 Jouandin, P., Marelja, Z., Shih, Y. H., Parkhitko, A. A., Dambowsky, M., Asara, J. M., Nemazanyy,  
874 I., Dibble, C. C., Simons, M., & Perrimon, N. (2022). Lysosomal cystine mobilization  
875 shapes the response of TORC1 and tissue growth to fasting. *Science*, 375(6582),  
876 eabc4203. <https://doi.org/10.1126/science.abc4203>

877 Jumper, J., Evans, R., Pritzel, A., Green, T., Figurnov, M., Ronneberger, O., Tunyasuvunakool, K.,  
878 Bates, R., Zidek, A., Potapenko, A., Bridgland, A., Meyer, C., Kohl, S. A. A., Ballard, A. J.,  
879 Cowie, A., Romera-Paredes, B., Nikolov, S., Jain, R., Adler, J., . . . Hassabis, D. (2021).  
880 Highly accurate protein structure prediction with AlphaFold. *Nature*, 596(7873), 583-589.  
881 <https://doi.org/10.1038/s41586-021-03819-2>

882 Kalatzis, V., Cherqui, S., Antignac, C., & Gasnier, B. (2001). Cystinosin, the protein defective in  
883 cystinosis, is a H(+) -driven lysosomal cystine transporter. *EMBO J*, 20(21), 5940-5949.  
884 <https://doi.org/10.1093/emboj/20.21.5940>

885 Kane, P. M. (1995). Disassembly and reassembly of the yeast vacuolar H(+) -ATPase *in vivo*. *J Biol  
886 Chem*, 270(28), 17025-17032. <https://www.ncbi.nlm.nih.gov/pubmed/7622524>

887 Kang, D. S., Tian, X., & Benovic, J. L. (2014). Role of beta-arrestins and arrestin domain-  
888 containing proteins in G protein-coupled receptor trafficking. *Curr Opin Cell Biol*, 27, 63-  
889 71. <https://doi.org/10.1016/j.ceb.2013.11.005>

890 Kenyon, C., Chang, J., Gensch, E., Rudner, A., & Tabtiang, R. (1993). A *C. elegans* mutant that  
891 lives twice as long as wild type. *Nature*, 366(6454), 461-464.  
892 <https://doi.org/10.1038/366461a0>

893 Khan, A. S., & Frigo, D. E. (2017). A spatiotemporal hypothesis for the regulation, role, and  
894 targeting of AMPK in prostate cancer. *Nat Rev Urol*, 14(3), 164-180.  
895 <https://doi.org/10.1038/nrurol.2016.272>

896 Lapierre, L. R., Gelino, S., Melendez, A., & Hansen, M. (2011). Autophagy and lipid metabolism  
897 coordinately modulate life span in germline-less *C. elegans*. *Curr Biol*, 21(18), 1507-1514.  
898 <https://doi.org/10.1016/j.cub.2011.07.042>

899 Laqtom, N. N., Dong, W., Medoh, U. N., Cangelosi, A. L., Dharamdasani, V., Chan, S. H., Kunchok,  
900 T., Lewis, C. A., Heinze, I., Tang, R., Grimm, C., Dang Do, A. N., Porter, F. D., Ori, A.,  
901 Sabatini, D. M., & Abu-Remaileh, M. (2022). CLN3 is required for the clearance of  
902 glycerophosphodiesters from lysosomes. *Nature*, 609(7929), 1005-1011.  
903 <https://doi.org/10.1038/s41586-022-05221-y>

904 Lawrence, R. E., & Zoncu, R. (2019). The lysosome as a cellular centre for signalling, metabolism  
905 and quality control. *Nat Cell Biol*, 21(2), 133-142. <https://doi.org/10.1038/s41556-018-0244-7>

907 Le, S., Josse, J., & Husson, F. (2008). FactoMineR: An R package for multivariate analysis. *Journal  
908 of statistical software*, 25(1), 1-18. <https://doi.org/10.18637/jss.v025.i01>

909 Leger-Silvestre, I., Caffrey, J. M., Dawaliby, R., Alvarez-Arias, D. A., Gas, N., Bertolone, S. J.,  
910 Gleizes, P. E., & Ellis, S. R. (2005). Specific Role for Yeast Homologs of the Diamond  
911 Blackfan Anemia-associated Rps19 Protein in Ribosome Synthesis. *J Biol Chem*, 280(46),  
912 38177-38185. <https://doi.org/10.1074/jbc.M506916200>

913 Li, R. J., Xu, J., Fu, C., Zhang, J., Zheng, Y. G., Jia, H., & Liu, J. O. (2016). Regulation of mTORC1 by  
914 lysosomal calcium and calmodulin. *Elife*, 5. <https://doi.org/10.7554/elife.19360>

915 Lin, H. J., Herman, P., Kang, J. S., & Lakowicz, J. R. (2001). Fluorescence lifetime characterization  
916 of novel low-pH probes. *Anal Biochem*, 294(2), 118-125.  
917 <https://doi.org/10.1006/abio.2001.5155>

918 Linkert, M., Rueden, C. T., Allan, C., Burel, J. M., Moore, W., Patterson, A., Loranger, B., Moore,  
919 J., Neves, C., Macdonald, D., Tarkowska, A., Sticco, C., Hill, E., Rossner, M., Eliceiri, K. W.,  
920 & Swedlow, J. R. (2010). Metadata matters: access to image data in the real world. *J Cell  
921 Biol*, 189(5), 777-782. <https://doi.org/10.1083/jcb.201004104>

922 Lubke, T., Lobel, P., & Sleat, D. E. (2009). Proteomics of the lysosome. *Biochim Biophys Acta*,  
923 1793(4), 625-635. <https://doi.org/10.1016/j.bbamcr.2008.09.018>

924 Ma, Z., Thomas, K. S., Webb, D. J., Moravec, R., Salicioni, A. M., Mars, W. M., & Gonias, S. L.  
925 (2002). Regulation of Rac1 activation by the low density lipoprotein receptor-related  
926 protein. *J Cell Biol*, 159(6), 1061-1070. <https://doi.org/10.1083/jcb.200207070>

927 Mak, K. H., Zhao, Q., Hu, P.-W., Au-Yeung, C.-L., Yang, J., Duraine, L., Yu, Y., Abu-Remaileh, M.,  
928 Sabatini, D., Wang, J. D., & Wang, M. C. (2020). Lysosomal nucleotide metabolism  
929 regulates ER proteostasis through mTOR signaling. *bioRxiv*, 2020.2004.2018.048561.  
930 <https://doi.org/10.1101/2020.04.18.048561>

931 Markmann, S., Krambeck, S., Hughes, C. J., Mirzaian, M., Aerts, J. M., Saftig, P., Schweizer, M.,  
932 Vissers, J. P., Braulke, T., & Damme, M. (2017). Quantitative Proteome Analysis of  
933 Mouse Liver Lysosomes Provides Evidence for Mannose 6-phosphate-independent  
934 Targeting Mechanisms of Acid Hydrolases in Mucolipidosis II. *Mol Cell Proteomics*, 16(3),  
935 438-450. <https://doi.org/10.1074/mcp.M116.063636>

936 Martins, R., Lithgow, G. J., & Link, W. (2016). Long live FOXO: unraveling the role of FOXO  
937 proteins in aging and longevity. *Aging Cell*, 15(2), 196-207.  
938 <https://doi.org/10.1111/ace.12427>

939 Mayer, M. P. (2010). Gymnastics of molecular chaperones. *Mol Cell*, 39(3), 321-331.  
940 <https://doi.org/10.1016/j.molcel.2010.07.012>

941 McGuire, C. M., & Forgac, M. (2018). Glucose starvation increases V-ATPase assembly and  
942 activity in mammalian cells through AMP kinase and phosphatidylinositol 3-kinase/Akt  
943 signaling. *J Biol Chem*, 293(23), 9113-9123. <https://doi.org/10.1074/jbc.RA117.001327>

944 Mijaljica, D., & Devenish, R. J. (2013). Nucleophagy at a glance. *J Cell Sci*, 126(Pt 19), 4325-4330.  
945 <https://doi.org/10.1242/jcs.133090>

946 Mutlu, A. S., Gao, S. M., Zhang, H., & Wang, M. C. (2020). Olfactory specificity regulates lipid  
947 metabolism through neuroendocrine signaling in *Caenorhabditis elegans*. *Nature  
948 communications*, 11(1), 1-15. <https://doi.org/10.1038/s41467-020-15296-8>

949 Nakae, I., Fujino, T., Kobayashi, T., Sasaki, A., Kikko, Y., Fukuyama, M., Gengyo-Ando, K., Mitani,  
950 S., Kontani, K., & Katada, T. (2010). The arf-like GTPase Arl8 mediates delivery of  
951 endocytosed macromolecules to lysosomes in *Caenorhabditis elegans*. *Mol Biol Cell*,  
952 21(14), 2434-2442. <https://doi.org/10.1091/mbc.E09-12-1010>

953 Nakamura, S., & Yoshimori, T. (2018). Autophagy and Longevity. *Mol Cells*, 41(1), 65-72.  
954 <https://doi.org/10.14348/molcells.2018.2333>

955 Navarro-Romero, A., Montpeyro, M., & Martinez-Vicente, M. (2020). The Emerging Role of the  
956 Lysosome in Parkinson's Disease. *Cells*, 9(11). <https://doi.org/10.3390/cells9112399>

957 Nicoli, E. R., Weston, M. R., Hackbarth, M., Becerril, A., Larson, A., Zein, W. M., Baker, P. R., 2nd,  
958 Burke, J. D., Dorward, H., Davids, M., Huang, Y., Adams, D. R., Zerfas, P. M., Chen, D.,  
959 Markello, T. C., Toro, C., Wood, T., Elliott, G., Vu, M., . . . Malicdan, M. C. V. (2019).  
960 Lysosomal Storage and Albinism Due to Effects of a *De Novo* CLCN7 Variant on  
961 Lysosomal Acidification. *Am J Hum Genet*, 104(6), 1127-1138.  
962 <https://doi.org/10.1016/j.ajhg.2019.04.008>

963 Nishimura, T., Kaizuka, T., Cadwell, K., Sahani, M. H., Saitoh, T., Akira, S., Virgin, H. W., &  
964 Mizushima, N. (2013). FIP200 regulates targeting of Atg16L1 to the isolation membrane.  
965 *EMBO Rep*, 14(3), 284-291. <https://doi.org/10.1038/embor.2013.6>

966 Nixon, R. A., & Cataldo, A. M. (2006). Lysosomal system pathways: genes to neurodegeneration  
967 in Alzheimer's disease. *J Alzheimers Dis*, 9(3 Suppl), 277-289.  
968 <https://doi.org/10.3233/jad-2006-9s331>

969 Pettersen, E. F., Goddard, T. D., Huang, C. C., Couch, G. S., Greenblatt, D. M., Meng, E. C., &  
970 Ferrin, T. E. (2004). UCSF Chimera--a visualization system for exploratory research and  
971 analysis. *J Comput Chem*, 25(13), 1605-1612. <https://doi.org/10.1002/jcc.20084>

972 Platt, F. M., Boland, B., & van der Spoel, A. C. (2012). The cell biology of disease: lysosomal  
973 storage disorders: the cellular impact of lysosomal dysfunction. *J Cell Biol*, 199(5), 723-  
974 734. <https://doi.org/10.1083/jcb.201208152>

975 Popovic, D., & Dikic, I. (2014). TBC1D5 and the AP2 complex regulate ATG9 trafficking and  
976 initiation of autophagy. *EMBO Rep*, 15(4), 392-401.  
977 <https://doi.org/10.1002/embr.201337995>

978 Pu, J., Guardia, C. M., Keren-Kaplan, T., & Bonifacino, J. S. (2016). Mechanisms and functions of  
979 lysosome positioning. *J Cell Sci*, 129(23), 4329-4339. <https://doi.org/10.1242/jcs.196287>

980 Ramachandran, P. V., Savini, M., Folick, A. K., Hu, K., Masand, R., Graham, B. H., & Wang, M. C.  
981 (2019). Lysosomal Signaling Promotes Longevity by Adjusting Mitochondrial Activity. *Dev  
982 Cell*, 48(5), 685-696 e685. <https://doi.org/10.1016/j.devcel.2018.12.022>

983 Ratto, E., Chowdhury, S. R., Siefert, N. S., Schneider, M., Wittmann, M., Helm, D., & Palm, W.  
984 (2022). Direct control of lysosomal catabolic activity by mTORC1 through regulation of  
985 V-ATPase assembly. *Nat Commun*, 13(1), 4848. <https://doi.org/10.1038/s41467-022-32515-6>

986 Rebsamen, M., Pochini, L., Stasyk, T., de Araujo, M. E., Galluccio, M., Kandasamy, R. K., Snijder,  
987 B., Fauster, A., Rudashevskaya, E. L., Bruckner, M., Scorzoni, S., Filipek, P. A., Huber, K. V.,  
988 Bigenzahn, J. W., Heinz, L. X., Kraft, C., Bennett, K. L., Indiveri, C., Huber, L. A., & Superti-  
989 Furga, G. (2015). SLC38A9 is a component of the lysosomal amino acid sensing  
990 machinery that controls mTORC1. *Nature*, 519(7544), 477-481.  
991 <https://doi.org/10.1038/nature14107>

992 Saltzman, A. B., Leng, M., Bhatt, B., Singh, P., Chan, D. W., Dobrolecki, L., Chandrasekaran, H.,  
993 Choi, J. M., Jain, A., Jung, S. Y., Lewis, M. T., Ellis, M. J., & Malovannaya, A. (2018).  
994 gpGrouper: A Peptide Grouping Algorithm for Gene-Centric Inference and Quantitation  
995 of Bottom-Up Proteomics Data. *Mol Cell Proteomics*, 17(11), 2270-2283.  
996 <https://doi.org/10.1074/mcp.TIR118.000850>

997 Savini, M., Folick, A., Lee, Y. T., Jin, F., Cuevas, A., Tillman, M. C., Duffy, J. D., Zhao, Q., Neve, I. A.,  
998 Hu, P. W., Yu, Y., Zhang, Q., Ye, Y., Mair, W. B., Wang, J., Han, L., Ortlund, E. A., & Wang,  
999 M. C. (2022). Lysosome lipid signalling from the periphery to neurons regulates  
1000 longevity. *Nat Cell Biol*, 24(6), 906-916. <https://doi.org/10.1038/s41556-022-00926-8>

1001 Savini, M., Zhao, Q., & Wang, M. C. (2019). Lysosomes: Signaling Hubs for Metabolic Sensing  
1002 and Longevity. *Trends Cell Biol*, 29(11), 876-887.  
1003 <https://doi.org/10.1016/j.tcb.2019.08.008>

1004 Schroder, B. A., Wrocklage, C., Hasilik, A., & Saftig, P. (2010). The proteome of lysosomes.  
1005 *Proteomics*, 10(22), 4053-4076. <https://doi.org/10.1002/pmic.201000196>

1006 Snyder, J. C., Rochelle, L. K., Lyerly, H. K., Caron, M. G., & Barak, L. S. (2013). Constitutive  
1007 Internalization of the Leucine-rich G Protein-coupled Receptor-5 (LGR5) to the Trans-  
1008 Golgi Network. *Journal of Biological Chemistry*, 288(15), 10286-10297.  
1009 <https://doi.org/10.1074/jbc.M112.447540>

1010 Stiernagle, T. (2006). Maintenance of *C. elegans*. *WormBook*, 1-11.  
1011 <https://doi.org/10.1895/wormbook.1.101.1>

1012 Stransky, L. A., & Forgac, M. (2015). Amino Acid Availability Modulates Vacuolar H+-ATPase  
1013 Assembly. *J Biol Chem*, 290(45), 27360-27369.  
1014 <https://doi.org/10.1074/jbc.M115.659128>

1015 Sun, Y., Li, M., Zhao, D., Li, X., Yang, C., & Wang, X. (2020). Lysosome activity is modulated by  
1016 multiple longevity pathways and is important for lifespan extension in *C. elegans*. *eLife*, 9,  
1017 e55745. <https://doi.org/10.7554/eLife.55745>

1019 Turk, V., Stoka, V., Vasiljeva, O., Renko, M., Sun, T., Turk, B., & Turk, D. (2012). Cysteine  
1020 cathepsins: from structure, function and regulation to new frontiers. *Biochim Biophys  
1021 Acta*, 1824(1), 68-88. <https://doi.org/10.1016/j.bbapap.2011.10.002>

1022 Varadi, M., Anyango, S., Deshpande, M., Nair, S., Natassia, C., Yordanova, G., Yuan, D., Stroe, O.,  
1023 Wood, G., Laydon, A., Zidek, A., Green, T., Tunyasuvunakool, K., Petersen, S., Jumper, J.,  
1024 Clancy, E., Green, R., Vora, A., Lutfi, M., . . . Velankar, S. (2022). AlphaFold Protein  
1025 Structure Database: massively expanding the structural coverage of protein-sequence  
1026 space with high-accuracy models. *Nucleic Acids Res*, 50(D1), D439-D444.  
1027 <https://doi.org/10.1093/nar/gkab1061>

1028 Vasu, S., Shah, S., Orjalo, A., Park, M., Fischer, W. H., & Forbes, D. J. (2001). Novel vertebrate  
1029 nucleoporins Nup133 and Nup160 play a role in mRNA export. *J Cell Biol*, 155(3), 339-  
1030 354. <https://doi.org/10.1083/jcb.200108007>

1031 Wang, M. C., O'Rourke, E. J., & Ruvkun, G. (2008). Fat metabolism links germline stem cells and  
1032 longevity in *C. elegans*. *Science*, 322(5903), 957-960.  
1033 <https://doi.org/10.1126/science.1162011>

1034 Wang, S., Tsun, Z. Y., Wolfson, R. L., Shen, K., Wyant, G. A., Plovanich, M. E., Yuan, E. D., Jones, T.  
1035 D., Chantranupong, L., Comb, W., Wang, T., Bar-Peled, L., Zoncu, R., Straub, C., Kim, C.,  
1036 Park, J., Sabatini, B. L., & Sabatini, D. M. (2015). Metabolism. Lysosomal amino acid  
1037 transporter SLC38A9 signals arginine sufficiency to mTORC1. *Science*, 347(6218), 188-  
1038 194. <https://doi.org/10.1126/science.1257132>

1039 Webb, B. A., Aloisio, F. M., Charafeddine, R. A., Cook, J., Wittmann, T., & Barber, D. L. (2021).  
1040 pHLARE: a new biosensor reveals decreased lysosome pH in cancer cells. *Mol Biol Cell*,  
1041 32(2), 131-142. <https://doi.org/10.1091/mbc.E20-06-0383>

1042 Willett, R., Martina, J. A., Zewe, J. P., Wills, R., Hammond, G. R. V., & Puertollano, R. (2017).  
1043 TFEB regulates lysosomal positioning by modulating TMEM55B expression and JIP4  
1044 recruitment to lysosomes. *Nat Commun*, 8(1), 1580. [https://doi.org/10.1038/s41467-017-01871-z](https://doi.org/10.1038/s41467-<br/>1045 017-01871-z)

1046 Wyant, G. A., Abu-Remaileh, M., Wolfson, R. L., Chen, W. W., Freinkman, E., Danai, L. V., Vander  
1047 Heiden, M. G., & Sabatini, D. M. (2017). mTORC1 Activator SLC38A9 Is Required to Efflux  
1048 Essential Amino Acids from Lysosomes and Use Protein as a Nutrient. *Cell*, 171(3), 642-  
1049 654 e612. <https://doi.org/10.1016/j.cell.2017.09.046>

1050 Zhang, C. S., Jiang, B., Li, M., Zhu, M., Peng, Y., Zhang, Y. L., Wu, Y. Q., Li, T. Y., Liang, Y., Lu, Z.,  
1051 Lian, G., Liu, Q., Guo, H., Yin, Z., Ye, Z., Han, J., Wu, J. W., Yin, H., Lin, S. Y., & Lin, S. C.  
1052 (2014). The lysosomal v-ATPase-Ragulator complex is a common activator for AMPK and  
1053 mTORC1, acting as a switch between catabolism and anabolism. *Cell Metab*, 20(3), 526-  
1054 540. <https://doi.org/10.1016/j.cmet.2014.06.014>

1055

1056 **FIGURE LEGENDS**

1057

1058 **Figure 1. Rapid lysosome isolation coupled with proteomic profiling**

1059 (A) Schematic of the workflow for immunoprecipitation-based lysosome purification (Lyso-IP)  
1060 and mass-spectrometry based proteomic profiling to identify lysosome-enriched proteomes in *C.*  
1061 *elegans*.  
1062 (B) Example images of transgenic strains carrying LMP-1 Lyso-Tag (LMP-1::RFP-3 $\times$ HA) with  
1063 LysoTracker staining to mark lysosomes *in vivo*. Scale bar=5  $\mu$ m.  
1064 (C) Example images of beads carrying purified lysosomes from Lyso-IP with LysoTracker  
1065 staining to mark intact lysosomes *in vitro*. Scale bar=5  $\mu$ m.  
1066 (D) Western blot for protein markers of different subcellular compartments using purified  
1067 lysosomes (Lyso-IP), paired non-lysosomal fractions (Flow-through) or Pellet.  
1068 (E) PCA analysis of four independent biological replicates of Lyso-IP and Flow-through samples.  
1069

1070 **Figure 2. Systematic view of lysosome-enriched proteome**

1071 (A) Scatter plots showing candidate selection from four independent biological replicates in  
1072 proteomics analyses. Proteins with at least 10-fold higher levels in Lyso-IP samples than in flow-  
1073 through (FT) controls are highlighted with different colors based on repeated times in four  
1074 replicates.  
1075 (B) Scatter plot showing candidate selection with normalization to non-tagged controls using  
1076 wild-type worms. 216 proteins with over 2-fold higher levels in Lyso-IP samples than in non-  
1077 tagged controls are highlighted in red.  
1078 (C) Pie chart showing molecular function categories of lysosome-enriched proteins.  
1079 (D) The lysosomal enrichment ratio (Lyso-IP vs FT) for each subunit of lysosomal vacuolar  
1080 ATPase (v-ATPase) in four independent replicates is shown. Inserted scheme showing lysosomal  
1081 V-ATPase assembly.  
1082 (E) Pie chart showing subcellular location categories of lysosome-enriched proteins.

1083

1084 **Figure 3. Lysosomal proteome heterogeneity across tissues**

1085 (A) Example images of transgenic strains carrying Lyso-Tag (LMP-1::RFP-3×HA) driven by

1086 four different tissue-specific promoters. Scale bar=20  $\mu$ m.

1087 (B-E) Scatter plot showing the relative enrichment ratio for each of 216 lysosome-enriched

1088 proteins identified from whole-body LMP-1 Lyso-IP in comparison with tissue-specific LMP-1

1089 Lyso-IPs, hypodermis (B), muscle (C), intestine (D) and neuron (E). X axis, enrichment ratio

1090 tissue-specific vs. whole-body; Y axis, normalized protein abundance over LMP-1; each dot

1091 represents the average of three replicates.

1092 (F) Heatmap showing the relative enrichment of 216 lysosome-enriched proteins identified from

1093 whole-body LMP-1 Lyso-IP in comparison with tissue-specific LMP-1 Lyso-IPs. Group I,

1094 comparable ratios between whole-body and tissue-specific Lyso-IPs; Group II, increase in tissue-

1095 specific Lyso-IPs ( $p<0.05$  by student's t-test); Group III, decrease in tissue-specific Lyso-IPs

1096 ( $p<0.05$  by student's t-test); Group IV, absent in tissue-specific IPs.

1097

1098 **Figure 4. Lysosomal proteome in different pro-longevity models**

1099 (A) Scheme showing four different longevity regulatory mechanisms used in this study. Loss-of-

1100 function mutants (lf) of *isp-1*, *daf-2*, and *glp-1* reduce mitochondrial electron transport chain

1101 (ETC) complex III, insulin/IGF-1 signaling, and germline stem cell proliferation, respectively,

1102 leading to lifespan extension; while increasing lysosomal lipolysis by *lipl-4* transgenic

1103 overexpression (*lipl-4* Tg) promotes longevity.

1104 (B) Venn diagram showing the overlap between the lysosome-enriched proteomes from wild-

1105 type (WT) and *lipl-4* Tg worms.

1106 (C) Upset graph showing the distribution and overlap of lysosome-enriched proteins across the  
1107 four pro-longevity models. Inserted Venn diagram showing the overlaps between the lysosome-  
1108 enriched proteomes of WT worms and the long-lived *daf-2(lf)* and *isp-1(lf)* mutants.

1109

1110 **Figure 5. Increased enrichment of lysosomal proteins upon lysosomal lipolysis**

1111 (A) Normalized protein levels (z-score across samples) of autophagy-related components,  
1112 mTORC1 signaling factors, lysosomal v-ATPase V0, V1, and transporting accessory (TA)  
1113 subunits, lysosomal hydrolases and transporter proteins from LMP-1 Lyso-IP proteomic analyses  
1114 of WT, *lipl-4 Tg*, *daf-2(lf)*, *isp-1(lf)* worms grown at 20°C and WT and *glp-1(lf)* worms grown  
1115 at 25°C.

1116 (B) The lysosomal enrichment ratio (Lyso-IP vs FT) for two homologs of AMPK catalytic  
1117 subunits, AAK-1 and AAK-2 in WT, *lipl-4 Tg*, *daf-2(lf)*, *isp-1(lf)* and *glp-1(lf)* worms.

1118 (C) Reduction of AMPK using the loss-of-function mutant of *aak-2*, *aak-2(lf)* together with *aak-1*  
1119 RNAi knockdown decreases lifespan by 17% and 29% in the WT and *lipl-4 Tg* background,  
1120 respectively. As a result, the lifespan extension caused by *lipl-4 Tg* is reduced from 72% to 48%.  
1121 \*\*\*  $p < 0.001$  by Log-rank test. The lifespan data are also in Supplementary File 8.

1122

1123 **Figure 6. Enhanced lysosome-nucleus proximity contributing to longevity**

1124 (A) The percentage of proteins with different subcellular localization is compared between  
1125 lysosome-enriched proteomes from WT and *lipl-4 Tg* worms. \*  $p = 0.019$  by 2-sample test for  
1126 equality of proportions.

1127 (B) Heatmap showing the average levels of nucleoporin proteins NPP-6 and NPP-15 in Lyso-IP  
1128 (IP) and flow-through (FT) samples from WT, *lipl-4 Tg*, *daf-2(lf)*, and *isp-1(lf)* worms.

1129 (C, E) Representative images of intestinal cells in WT, *lipl-4 Tg* (C), and *daf-2(lf)* (E) worms  
1130 carrying LMP-1::RFP-3×HA and nucleus-enriched GFP, showing the accumulation of  
1131 lysosomes around the perinuclear region in the *lipl-4 Tg* but not *daf-2(lf)* worms. Dashed lines  
1132 circle intestinal cells and n marks the nucleus. Scale bar=20  $\mu$ m.  
1133 (D, F) Line graph showing the spatial distribution of lysosomes from the nuclear to peripheral  
1134 region quantified by normalized regional RFP fluorescence signals in intestinal cells of WT, *lipl-*  
1135 *4 Tg* (D), and *daf-2(lf)* (F) worms. N =50 WT /33 *lipl-4 Tg*, 33 WT/ 28 *daf-2(lf)*. Data are  
1136 represented as mean  $\pm$  SD. *p* values for (D) (from left to right): 1.23x10<sup>-7</sup>, 2.25x10<sup>-5</sup>, 0.00322,  
1137 0.368, 0.273, 0.0447, 0.00268, 1.20x10<sup>-5</sup>; *p* values for (F) (from left to right): 0.633, 0.0211,  
1138 0.00259, 0.0359, 0.767, 0.151, 0.106, 0.0671.  
1139 (G-H) *lipl-4 Tg* worms show lifespan extension compared to WT worms (G), which is fully  
1140 suppressed by RNAi knockdown of *npp-6* (H). \*\*\**p*<0.001, n.s. *p*>0.05 by Log-rank test.  
1141 (I-J) *daf-2(lf)* worms show lifespan extension compared to WT worms (I), which is not affected  
1142 by *npp-6* RNAi knockdown (J). \*\*\**p*<0.001 by Log-rank test.  
1143 The lifespan data are also in Supplementary File 8.  
1144  
1145 **Figure 7. Lysosome-enriched proteome identified with Cystinosin**  
1146 (A) Example images of transgenic strains carrying CTNS-1 Lyso-Tag (CTNS-1::RFP-3×HA)  
1147 with LysoTracker staining to mark lysosomes *in vivo*. Scale bar=5  $\mu$ m.  
1148 (B) Venn diagram showing the overlap between lysosome-enriched proteomes using LMP-1  
1149 Lyso-IP and CTNS-1 Lyso-IP.  
1150 (C) Pie chart showing subcellular location categories of lysosome-enriched proteins.

1151 (D) The proportion of candidates with lysosomal localization annotation in different candidate  
1152 groups. “LMP-1 all” and “CTNS-1 all”, all candidates from LMP-1 Lyso-IP and CTNS-1 Lyso-  
1153 IP, respectively; “LMP-1 only” and “CTNS-1 only”, candidates only identified from LMP-1  
1154 Lyso-IP or CTNS-1 Lyso-IP, respectively.  
1155 (E) Normalized protein levels (z-score across samples) of autophagy-related components and  
1156 mTORC1 signaling factors from CTNS-1 Lyso-IP proteomic analyses of WT worms and LMP-1  
1157 Lyso-IP proteomic analyses of WT and *lipl-4* *Tg* worms.  
1158 (F) Representative muscle images in the wrmScarlet::LMTR-3 knock-in line crossed with either  
1159 LMP-1::mNeonGreen knock-in line or CTNS-1::mNeonGreen knock-in line. Scale bar=20  $\mu$ m.  
1160 (G) Normalized protein levels (z-score across samples) of previously annotated lysosomal  
1161 proteins from LMP-1 Lyso-IP proteomic analyses of WT and *lipl-4* *Tg* worms and CTNS-1  
1162 Lyso-IP proteomic analyses of WT worms.

1163  
1164 **Figure 8. Lysosome-enriched proteins regulating lysosomal functions**  
1165 (A-E) Confocal fluorescence microscopy images of intestinal cells in worms stained with  
1166 LysoSensor DND-189 and treated with *empty vector* (A), *slc36.2* RNAi (B), *R144.6* RNAi (C),  
1167 *vha-5* RNAi (D) and *unc-32* RNAi (E). Scale bar=50  $\mu$ m.  
1168 (F, G) RNAi knockdown of *unc-32* or *vha-5* decreases the lysosome number (\*\*p<0.0001) (F)  
1169 but increases the lysosome size (\*\*\*\*p<0.0001, \*\*\* p<0.001) (G). The average lysosome  
1170 number and size per pair of intestinal cells were quantified. Data are shown as mean  $\pm$  standard  
1171 deviation (SD). Student *t*-test (unpaired, two-tailed) was performed between the *empty vector*  
1172 and RNAi-treated groups. At least three independent experiments with ~ 10 worms in each were  
1173 performed for each condition. n.s. p>0.05,

1174 (H) RNAi knockdown of *R144.6* and *unc-32* (\*\* $p < 0.001$ ) increase and decrease lysosomal pH,  
1175 respectively. Lysosomal pH was calculated based on LysoSensor's lifetime measured by  
1176 Fluorescence Lifetime Microscopy. Data are shown as mean  $\pm$  SD. Student t-test (unpaired,  
1177 two-tailed) was performed between the *empty vector* and RNAi-treated groups. Two independent  
1178 experiments with at least 5 worms in each were performed in *R144.6* RNAi and *unc-32* RNAi  
1179 conditions. The *vha-5* and *slc36.2* RNAi knockdown did not show significant changes in one  
1180 replicate and were not retested with another replicate. n.s.  $p > 0.05$ .

1181 (I) The structure of the *R144.6* protein predicted by AlphaFold2 supports it as a solute carrier  
1182 family transporter.

1183 (J) Confocal fluorescence microscopy images show that mNeonGreen signals from  
1184 endogenously tagged *R144.6* colocalize with LysoTracker Red signals in the hypodermis. Scale  
1185 bar=10  $\mu$ m.

1186  
1187 **Figure 1-figure supplement 1. Analysis of *LysoTg* lines and Lyso-IP profiling in wild-type**  
1188 **worms**

1189 (A) Developmental timing of WT and transgenic strains expressing LMP-1 and CTNS-1 Lyso-  
1190 Tag (LMP-1 and CTNS-1 *LysoTg*). n.s.  $p > 0.05$  by Chi-squared test.

1191 (B) Lifespan of WT, LMP-1 *LysoTg*, and CTNS-1 *LysoTg* worms. The lifespan data are also in  
1192 Supplementary File 8.

1193 (C) Correlation analysis of four independent biological replicates of Lyso-IP (IP) and Flow-  
1194 through (FT) samples from proteomics analyses.

1195 **Figure 2-figure supplement 1. Pie chart showing the proportion of LMP-1 Lyso-IP**  
1196 **candidates from WT worms with mammalian homologs.**

1197

1198 **Figure 3-figure supplement 1. Tissue-specific Lyso-IPs and candidate imaging**

1199 **(A-D)** Pearson Correlation matrices of tissue-specific lyso-IP (IP) samples and flow-through (FT)  
1200 samples show the correlation among three different replicates. **(A)** Hypodermis, **(B)** Muscle, **(C)**  
1201 Intestine, **(D)** Neuron.

1202 **(E)** Representative images showing colocalization of Y58A7A.1::mNeonGreen and LysoTracker  
1203 Red in the hypodermis. Scale bar=20  $\mu$ m.

1204

1205 **Figure 4-figure supplement 1. Lyso-IP analyses from different long-lived strains.**

1206 **(A-D)** Correlation analysis of three independent biological replicates of Lyso-IP (IP) and Flow-  
1207 through (FT) from proteomics analyses of the long-lived *lipl-4* transgenic strain (*lipl-4 Tg*, **A**),  
1208 the *daf-2* loss-of-function mutant (*daf-2(lf)*), **B**), the *isp-1* loss-of-function mutant (*isp-1(lf)*), **C**)  
1209 and *glp-1* loss-of-function mutant grown in 25°C (*glp-1(lf)*) 25°C, **D**).

1210 **(E)** PCA analysis of Lyso-IP replicates (IP) and flow-through controls (FT) in LMP-1 Lyso-IP of  
1211 WT, *lipl-4 Tg*, *daf-2(lf)*, and *isp-1(lf)* worms.

1212 **(F)** PCA analysis of Lyso-IP replicates (IP) and flow-through controls (FT) in LMP-1 Lyso-IP of  
1213 WT and *glp-1(lf)* worms grown at 25°C.

1214 **(G)** Venn diagram showing the overlap between the lysosome-enriched proteomes from WT and  
1215 *glp-1(lf)* worms grown at 25°C.

1216 **(H)** Upset graph showing the overlap of lysosome-enriched proteins present in the long-lived  
1217 worms but absent from WT worms.

1218

1219 **Figure 6-figure supplement 1. Lysosomal positioning in longevity regulation**

1220 (A) Summary of the method flow for quantifying the lysosomal distribution in intestinal cells of  
1221 *C. elegans*. Scale bar=10  $\mu$ m.

1222 (B, C) Curve graph showing the normalized accumulated intensity of lysosomal signals from the  
1223 nuclear to the peripheral region in WT, *lipl-4 Tg* (B), and *daf-2(lf)* (C) animals.  $*p<0.05$ ;  
1224  $**p<0.01$ ,  $***p<0.001$ ,  $****p<0.0001$ , n.s.  $p>0.05$  by Student's t-test (unpaired, two-tailed) for  
1225 each region. N =50 WT /33 *lipl-4 Tg*, 33 WT/ 28 *daf-2(lf)*. Data are represented as mean  $\pm$  SD.  $p$   
1226 values for (B) (from left to right):  $2.65 \times 10^{-8}$ ,  $3.19 \times 10^{-8}$ ,  $7.93 \times 10^{-8}$ ,  $3.62 \times 10^{-7}$ ,  $4.79 \times 10^{-6}$ ,  $2.98$   
1227  $\times 10^{-5}$ ,  $4.41 \times 10^{-5}$ ;  $p$  values for (C) (from left to right): 0.357, 0.0529, 0.00611, 0.00246, 0.00985,  
1228 0.0261, 0.0423.

1229 (D-E) *isp-1(lf)* worms show lifespan extension compared to WT worms (D), which is not  
1230 affected by RNAi knockdown of *npp-6* (E).  $***p<0.001$  by Log-rank test.

1231 (F-H) *lipl-4 Tg* worms show lifespan extension compared to WT worms (F), which is not  
1232 affected by *xpo-1* RNAi knockdown (G) and is partially suppressed by RNAi knockdown of  
1233 *ima-3* (H).  $***p<0.001$  by Log-rank test.

1234 The lifespan data are also in Supplementary File 8.

1235 (I). The percentage of proteins with different subcellular localization is compared between  
1236 lysosome-enriched proteomes from WT and *daf-2* worms.

1237

1238 **Figure 7-figure supplement 1. The colocalization between LMP-1::mNeonGreen and**  
1239 **CTNS-1::wrmsScarlet in different tissues**

1240 Representative images of knock-in lines with both LMP-1::mNeonGreen and CTNS-  
1241 1::wrmsScarlet show partial colocalization between LMP-1 and CTNS-1 signals in different  
1242 tissues. Scale bar=20  $\mu$ m.

1243

1244 **Figure 7-figure supplement 2. CTNS-1 Lyso-IPs and LMTR-3 imaging analyses**

1245 (A) Correlation analysis of three independent biological replicates of CTNS-1 Lyso-IP (IP) and  
1246 Flow-through (FT).

1247 (B) PCA analysis of three independent biological replicates of CTNS-1 Lyso-IP (IP) and Flow-  
1248 through (FT).

1249 (C, D) Example images of knock-in lines with wrmScarlet::LMTR-3 and CTNS-1::mNeonGreen  
1250 (C) and LMP-1::mNeonGreen (D) in hypodermis and intestine. Scale bar=20  $\mu$ m.

1251

1252 **Figure 8-figure supplement 1. LysoSensor intensity quantification in five candidates**

1253 The LysoSensor signals are visualized by confocal fluorescence microscopy in *empty vector* (A),  
1254 *slc36.2* RNAi (B), *R144.6* RNAi (C), *vha-5* RNAi (D), and *unc-32* RNAi (E) conditions. Scale  
1255 bar=50  $\mu$ m. The relative LysoSensor changes were quantified in (F). ~ 10 worms were quantified  
1256 in each condition. Data are shown as mean  $\pm$  SD. Student t-test (unpaired, two-tailed) was  
1257 performed between the *empty vector* and RNAi-treated groups. (\*\* $p$ < 0.01, \*\*\* $p$ < 0.0001).

1258

1259 **Supplementary File 1. Lysosome-enriched proteins identified from LMP-1 Lyso-IP using  
1260 WT worms**

1261 **Supplementary File 2. Lysosome-enriched proteome exhibits tissue-specificity**

1262 **Supplementary File 3. Lysosome-enriched proteins identified from LMP-1 Lyso-IP using  
1263 *lpl-4* Tg worms**

1264 **Supplementary File 4. Lysosome-enriched proteins identified from LMP-1 Lyso-IP using  
1265 *daf-2(lf)* mutant**

1266 **Supplementary File 5. Lysosome-enriched proteins identified from LMP-1 Lyso-IP using**  
1267 ***isp-1(lf)* mutant**

1268 **Supplementary File 6. Lysosome-enriched proteins identified from LMP-1 Lyso-IP using**  
1269 ***glp-1(lf)* mutant in 25°C**

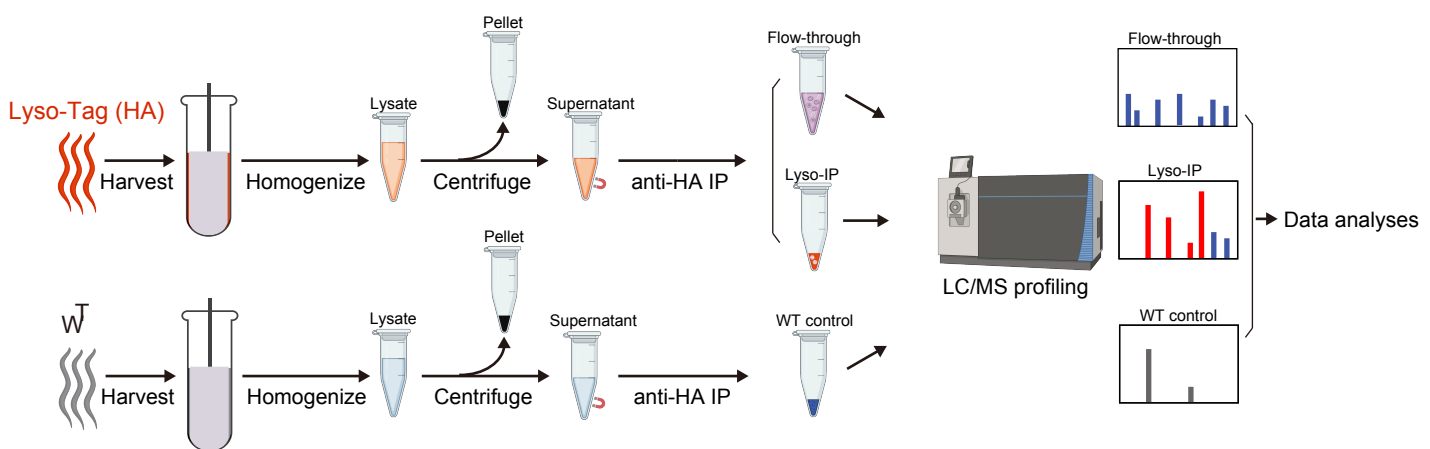
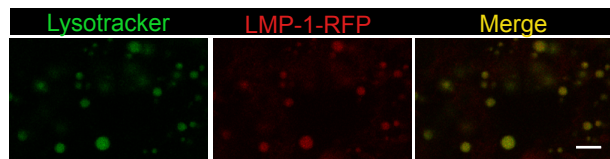
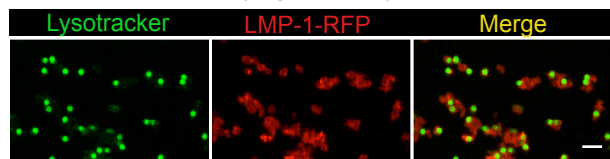
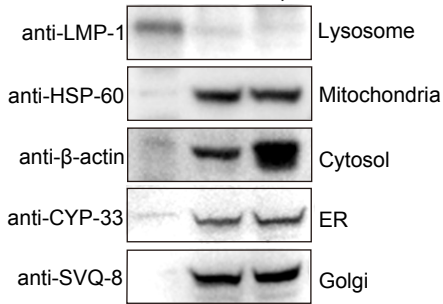
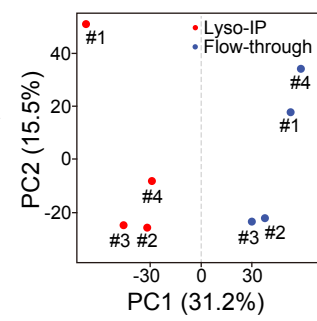
1270 **Supplementary File 7. Lysosome-enriched proteins identified from LMP-1 Lyso-IP using**  
1271 **WT worms in 25°C**

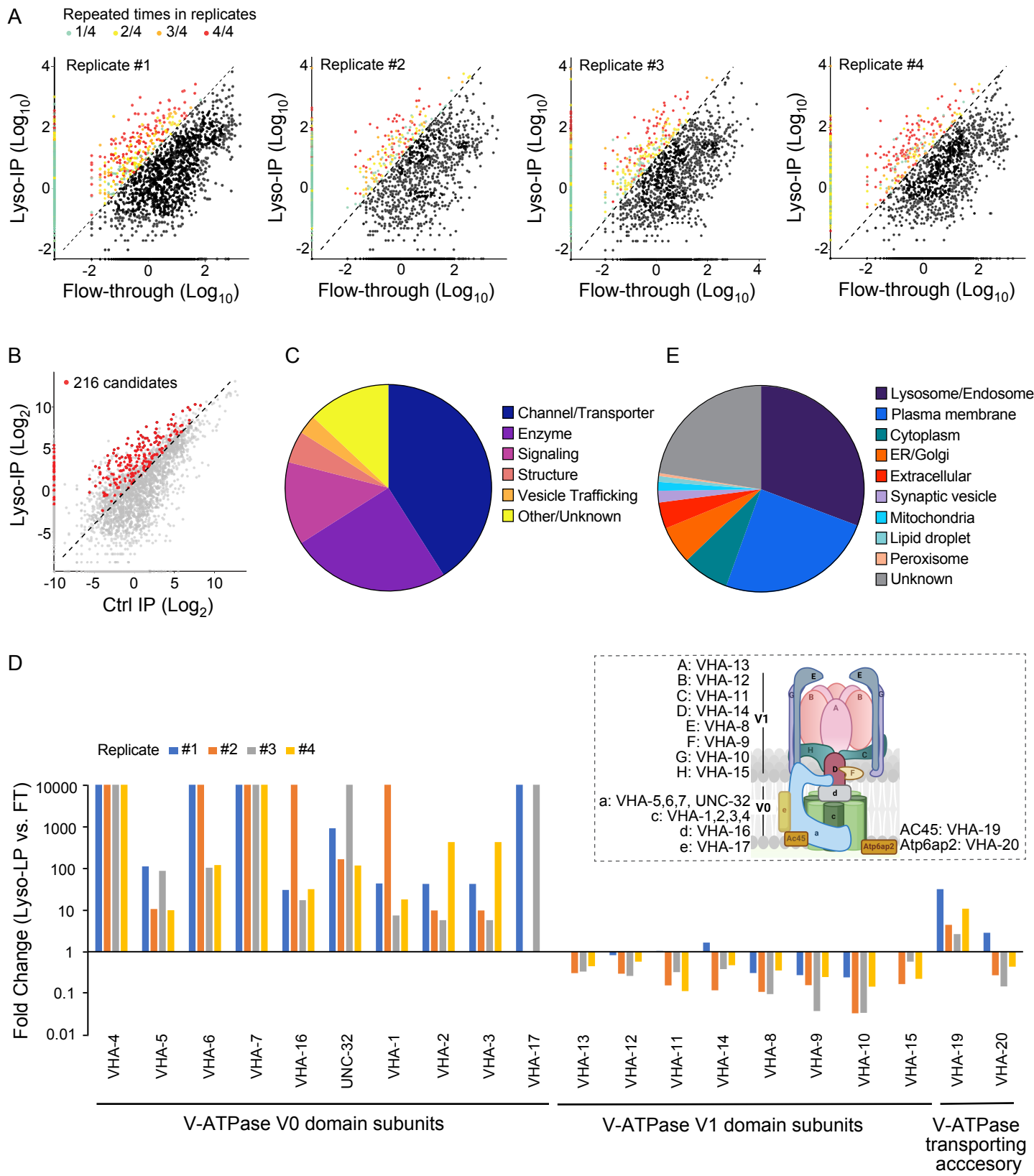
1272 **Supplementary File 8. Summary of lifespan analyses**

1273 **Supplementary File 9. Lysosome-enriched proteins identified from CTNS-1 Lyso-IP using**  
1274 **WT worms**

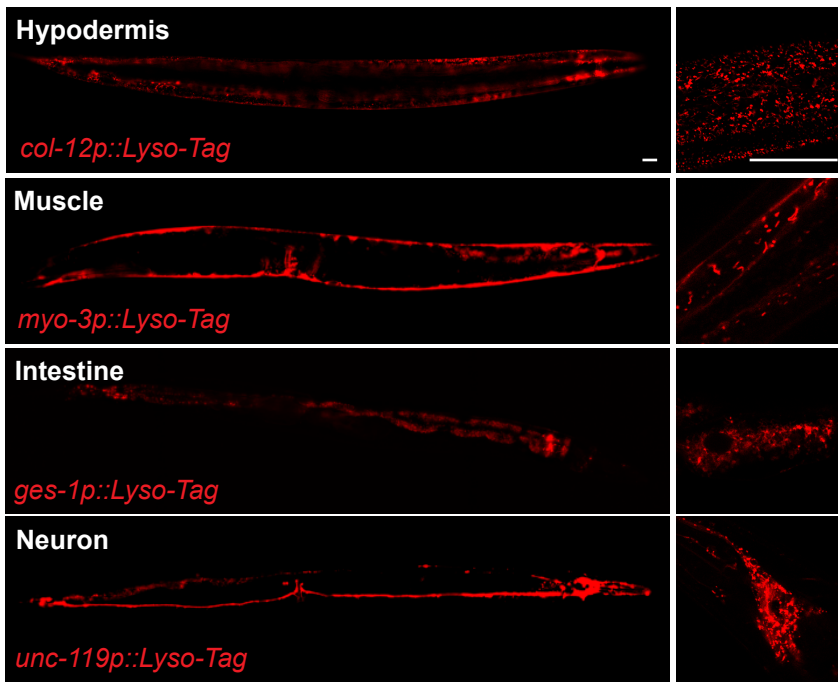
1275 **Supplementary File 10. LysoSensor screening of lysosome-enriched proteins shared**  
1276 **between LMP-1 and the CTNS-1 Lyso-IPs**

1277 **Source Code File 1. Matlab code for lysosome distribution quantification**

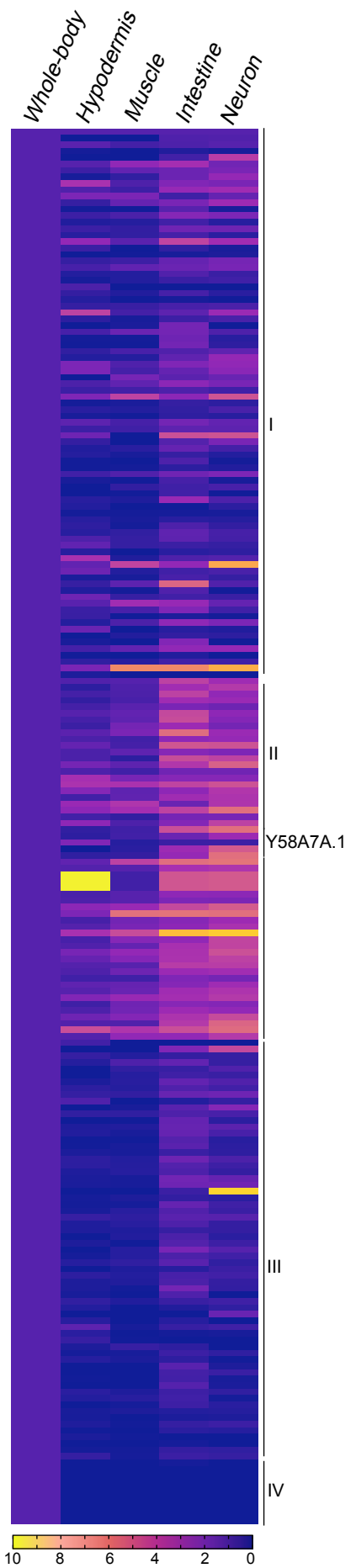
**A****B Worms carrying LMP-1::RFP::HA****C Beads carrying purified lysosomes****D**      **Lyso-IP**      **Flow-through**      **Pellet****E**



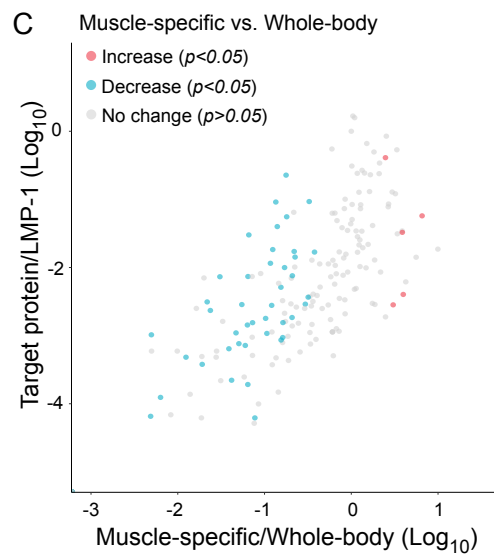
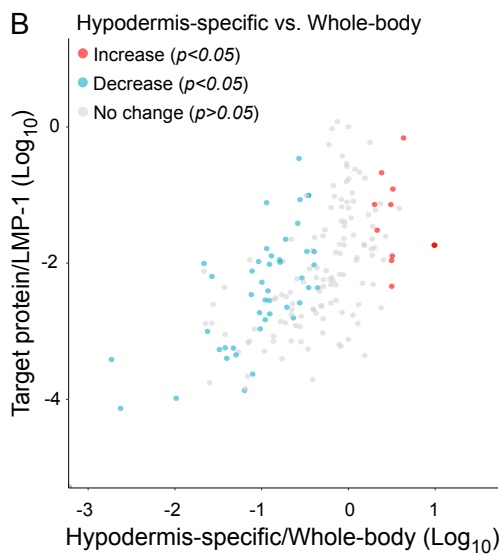
A



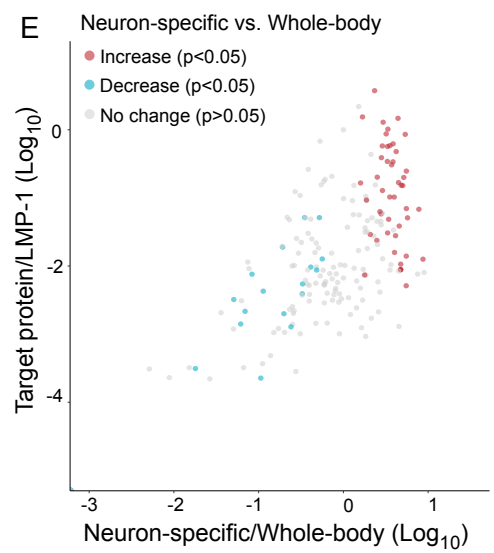
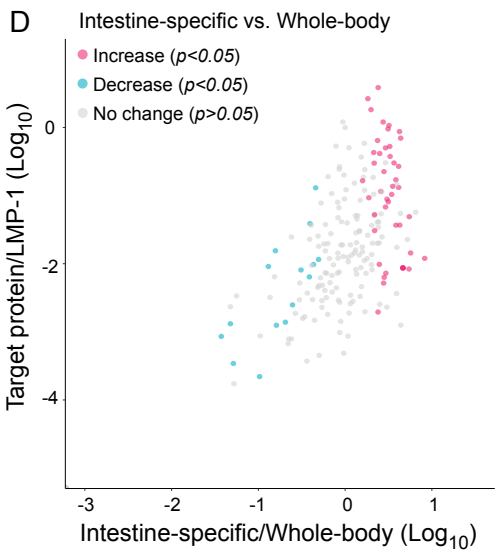
F

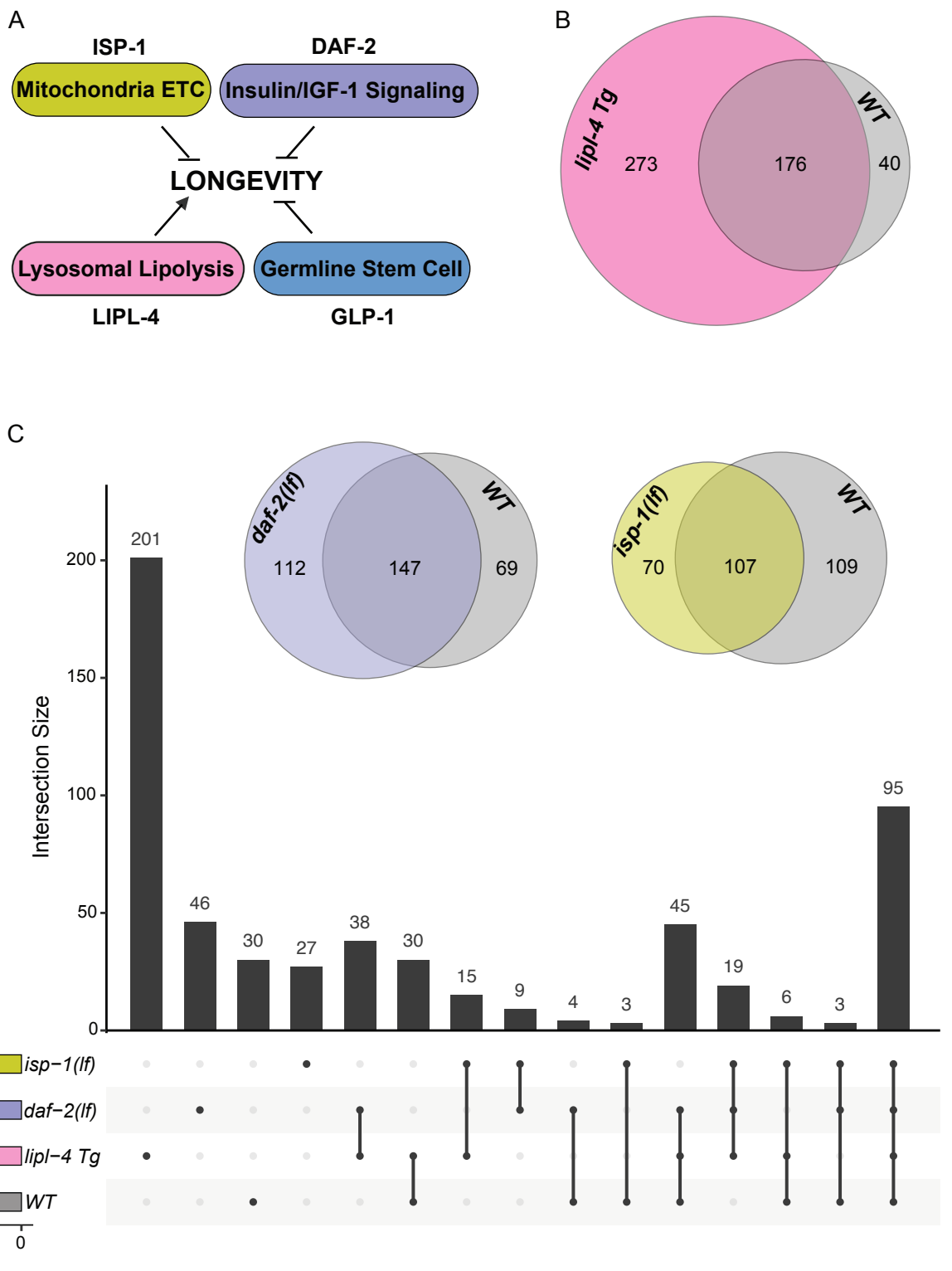


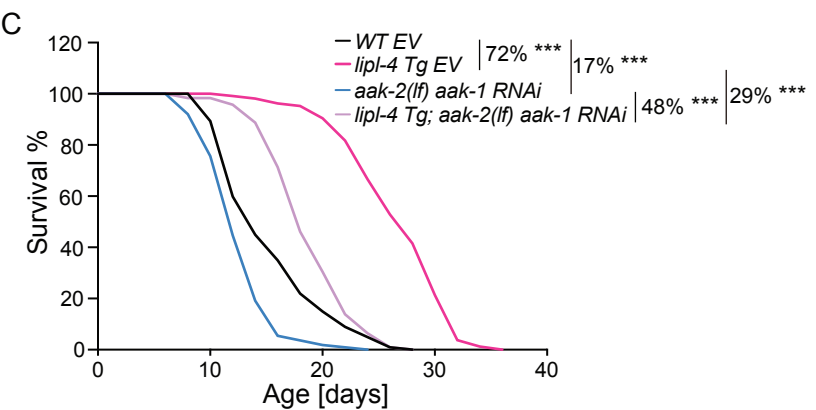
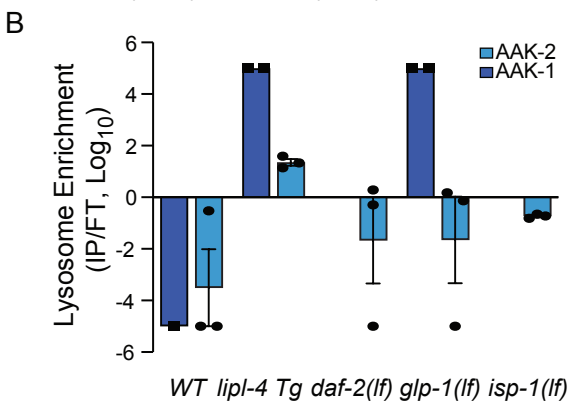
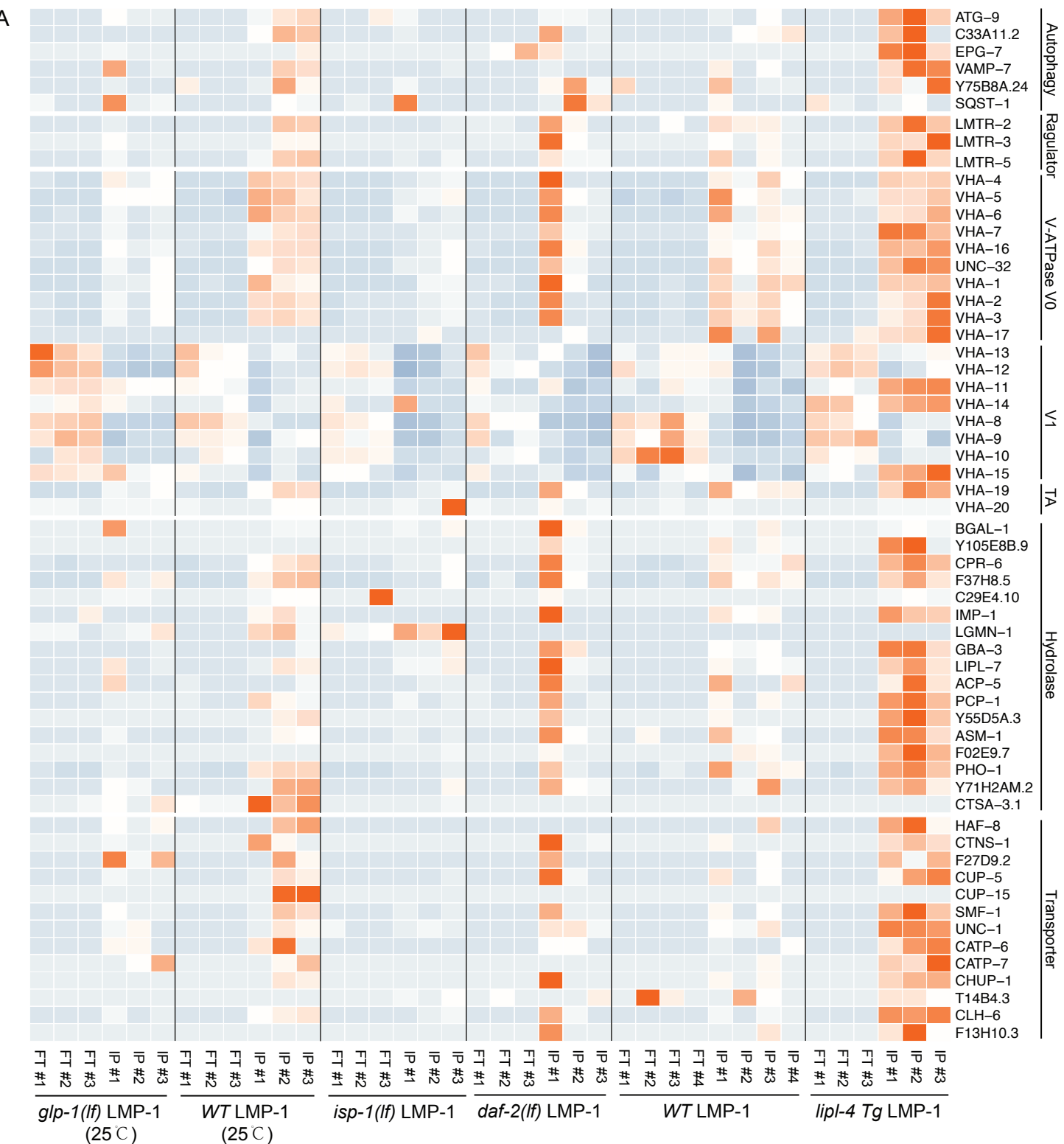
B

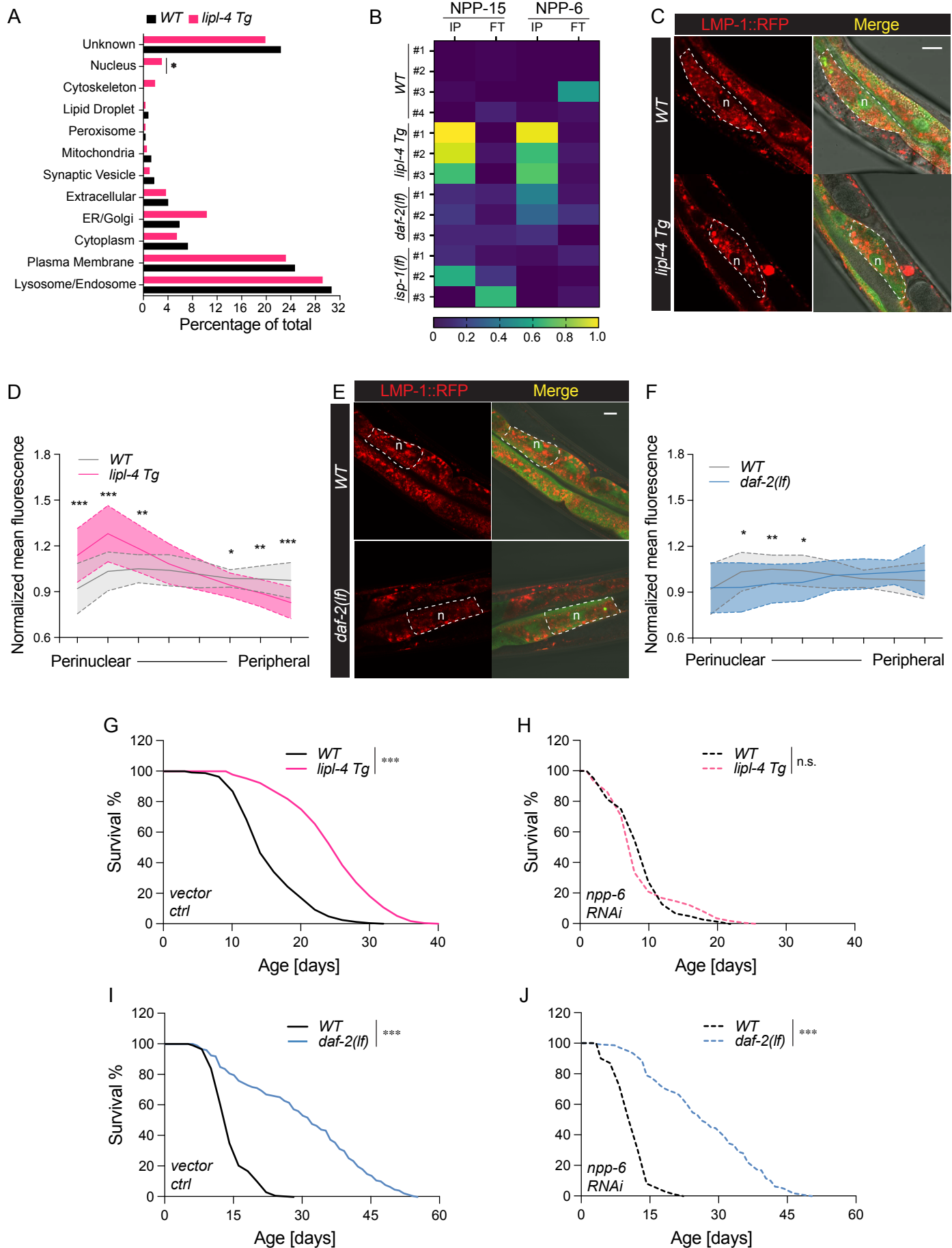


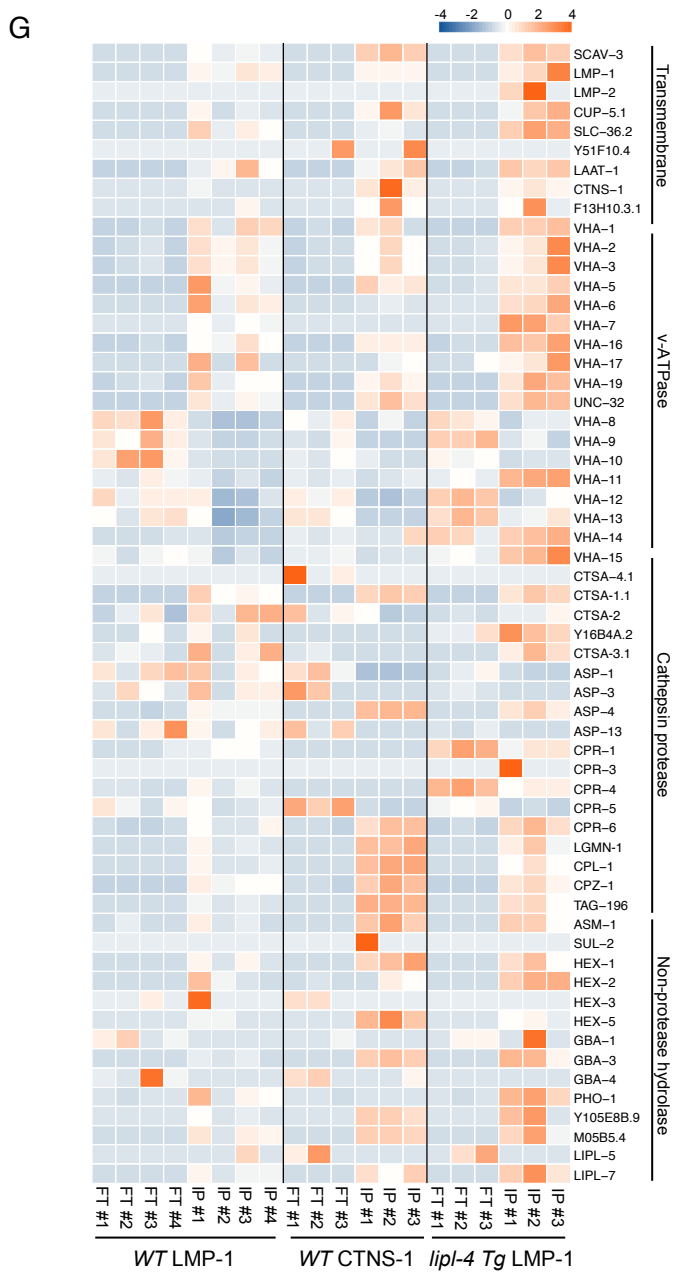
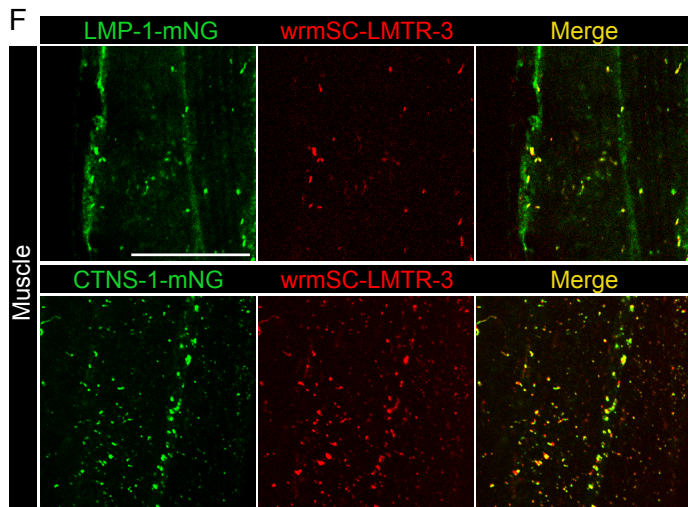
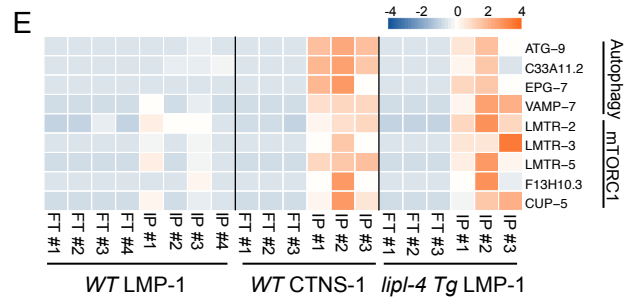
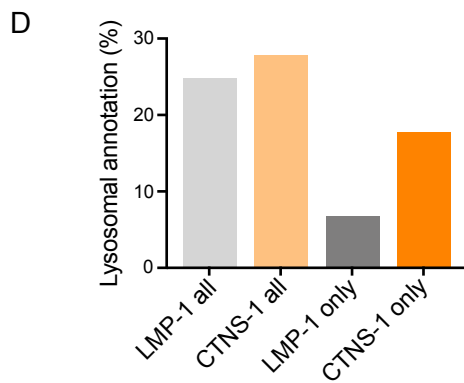
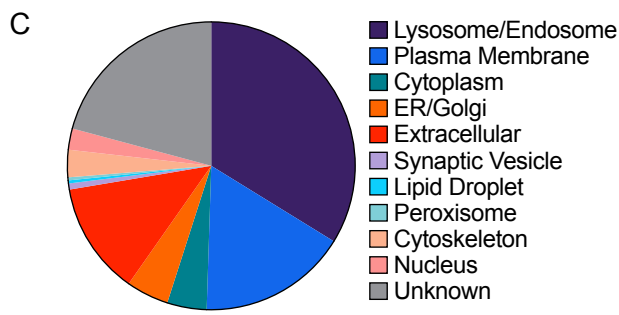
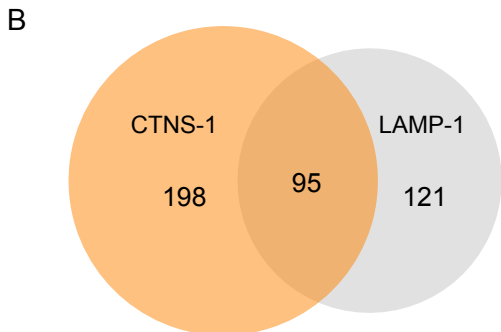
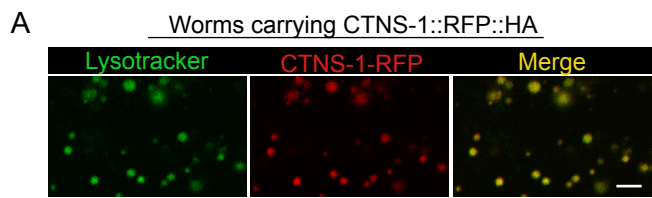
D

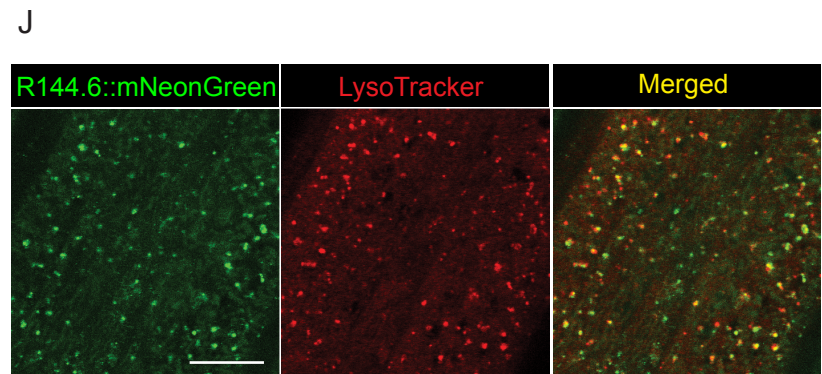
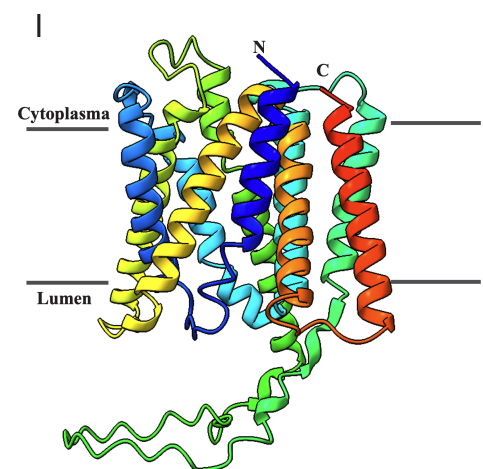
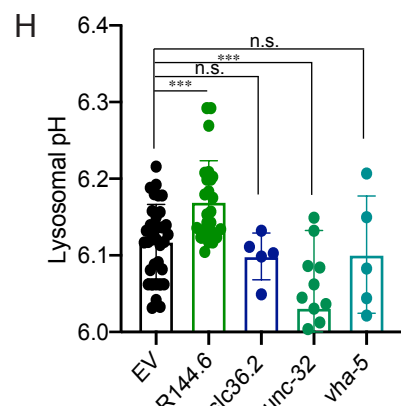
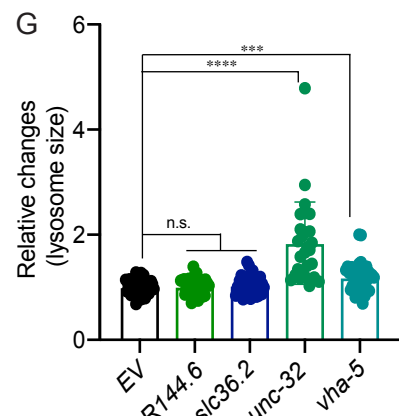
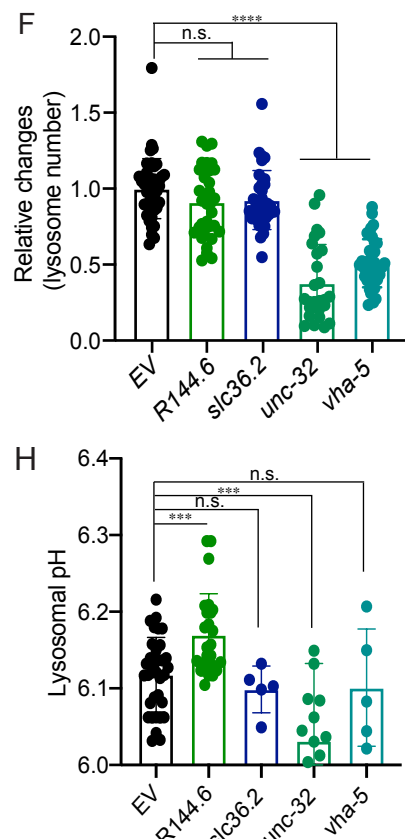
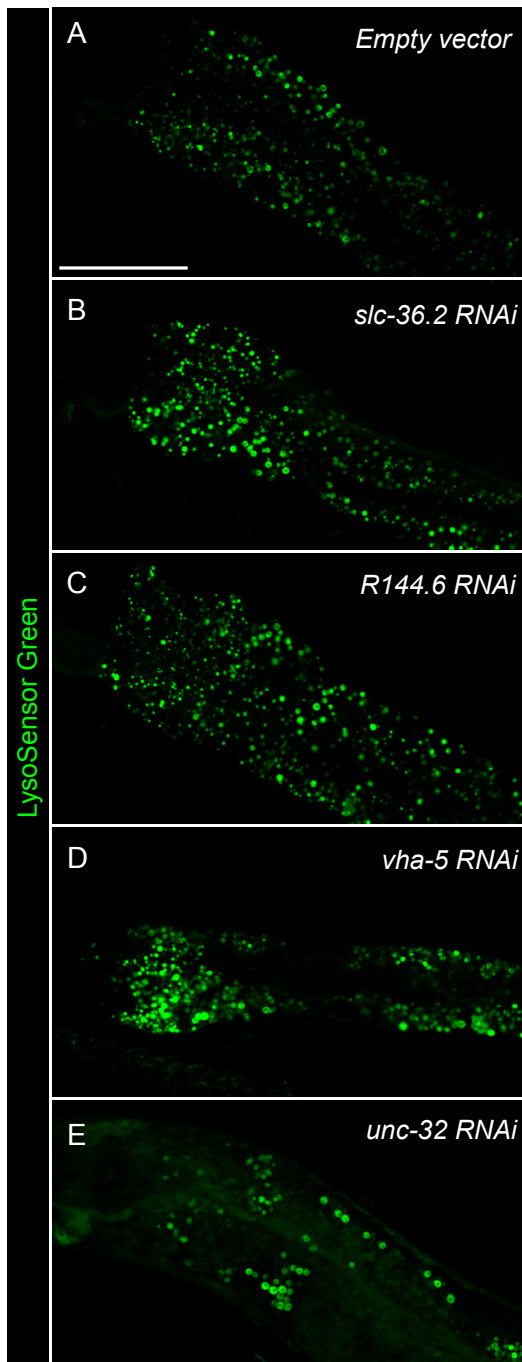


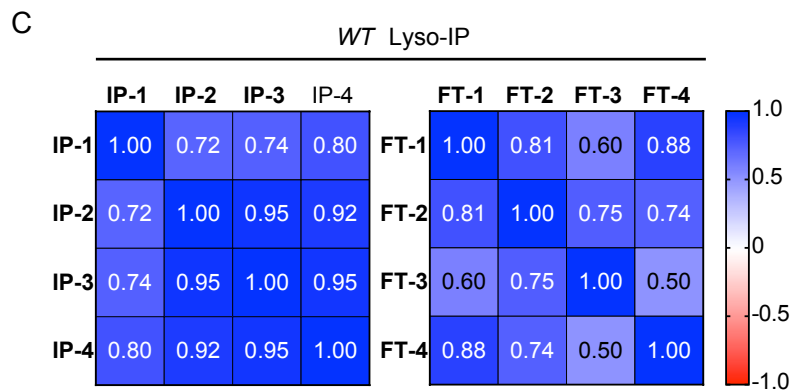
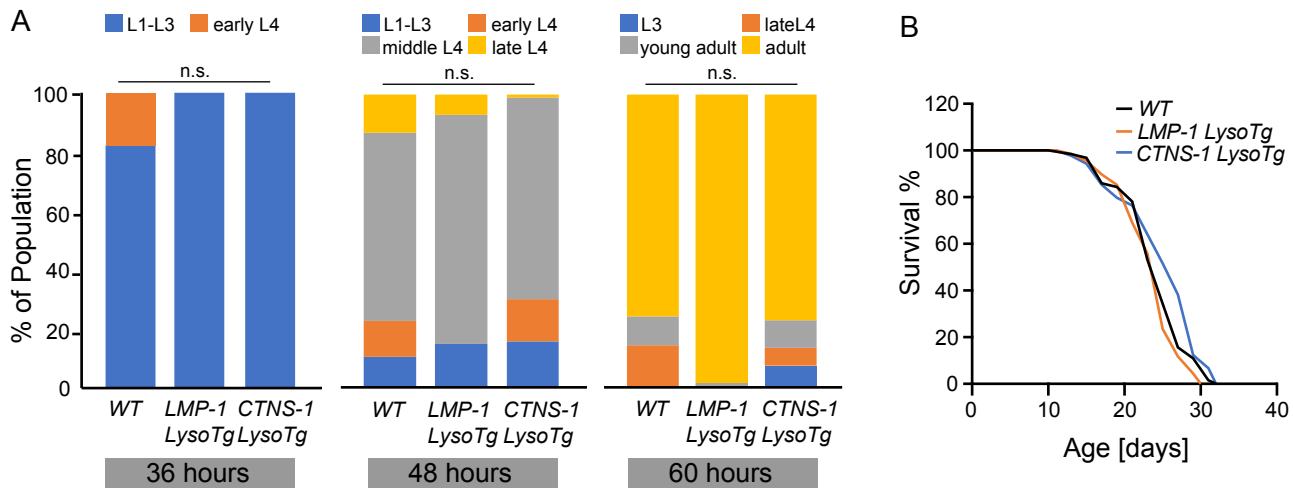


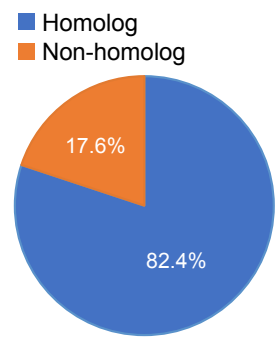


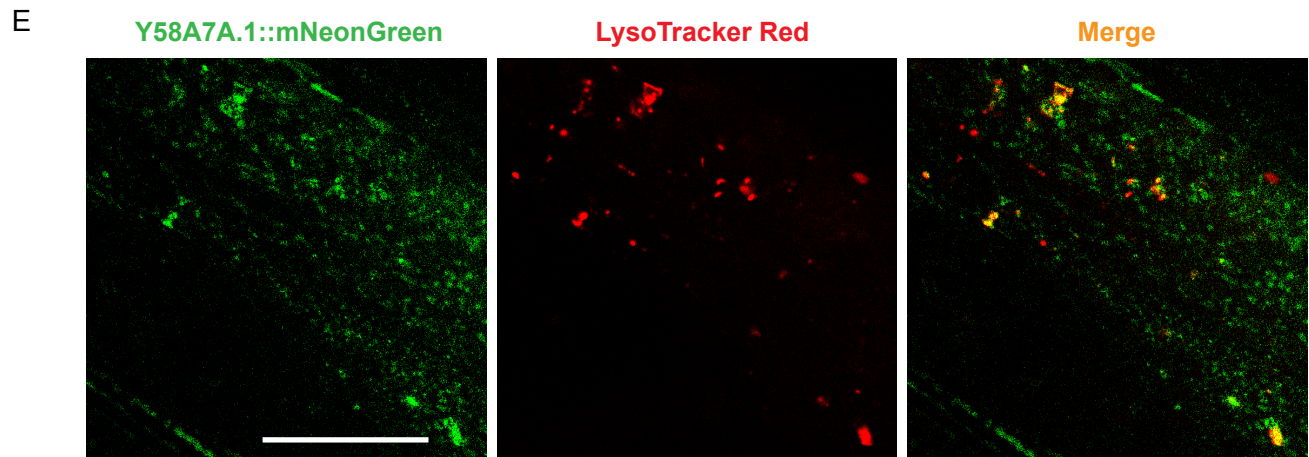
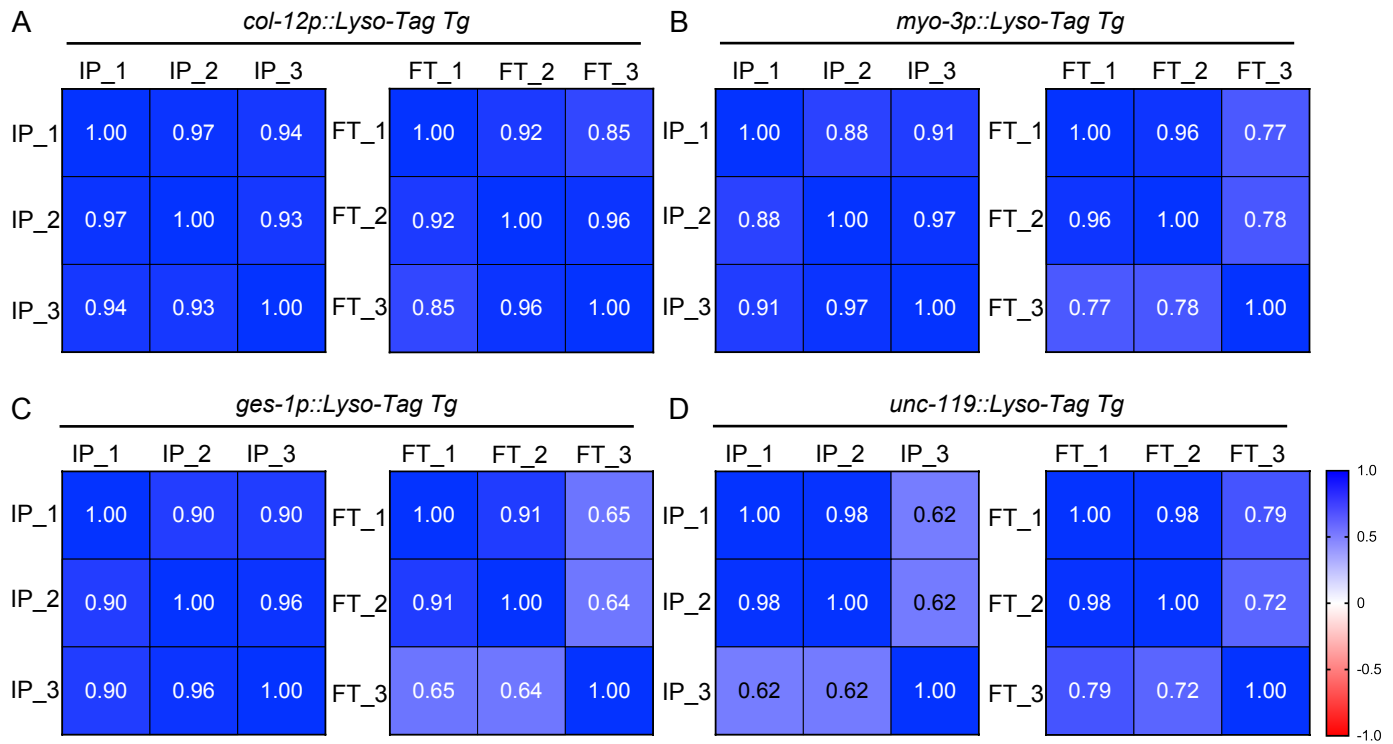


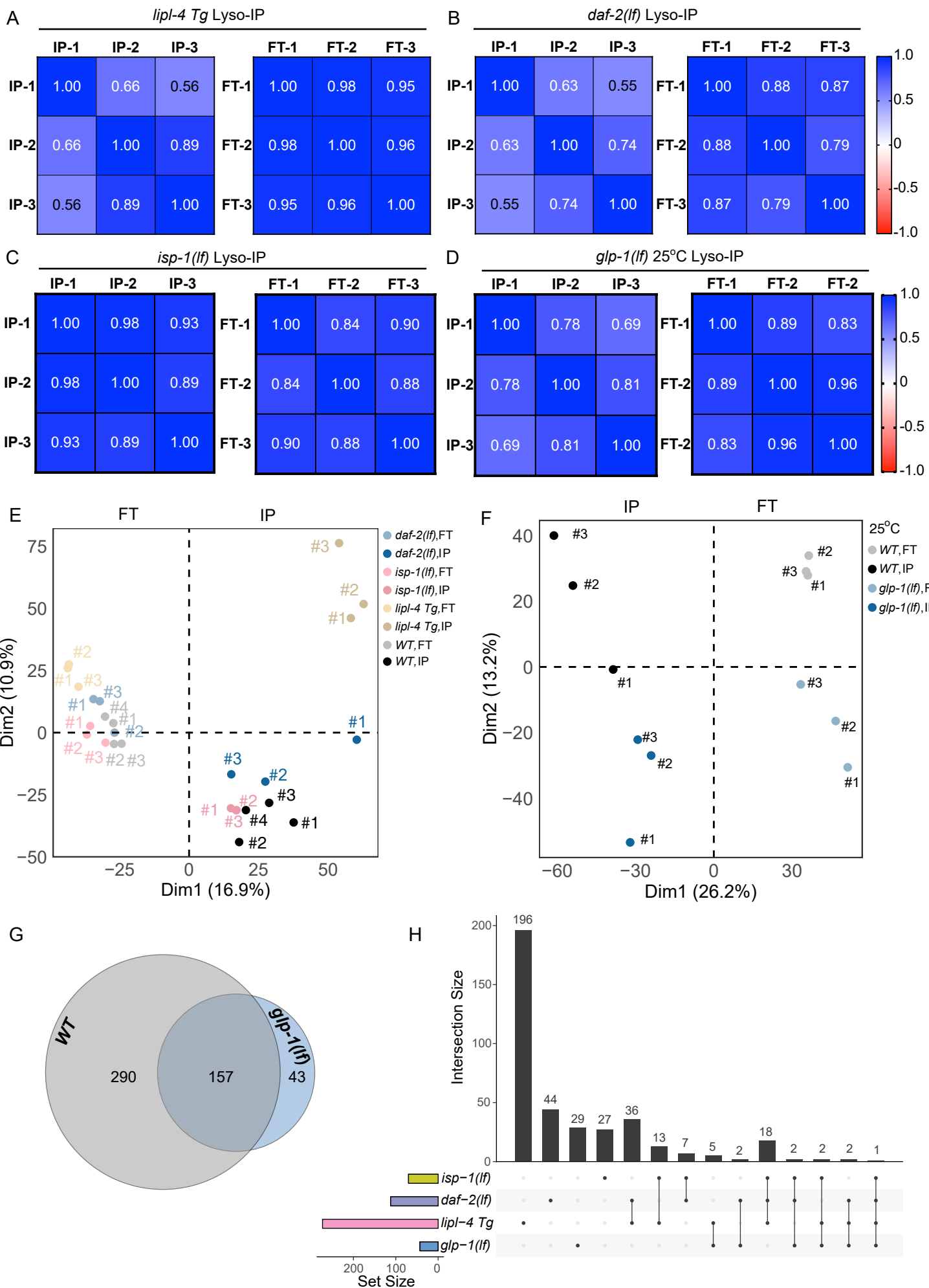












A Outline nuclear membrane → Outline plasma membrane → Regions divided

